

Optical Excitation of Semiconductor Nano-particles in Hollow-Core Fiber

by

Anna Maria Houk

A thesis
presented to the University of Waterloo
in fulfillment of the
thesis requirement for the degree of
Masters of Science
in
Electrical and Computer Engineering - Quantum Information

Waterloo, Ontario, Canada, 2022

© 2022

Author's Declaration

I hereby declare that I am the sole author of this thesis. This is a true copy of the thesis, including any required final revisions, as accepted by my examiners.

I understand that my thesis may be made electronically available to the public.

Abstract

This is the abstract.

Acknowledgements

I'd first like to thank Prof. Bacjsy, Prof. Tsen, and Prof. Kim for providing feedback on my thesis, and additionally Prof. Bajcsy for insights. I'd also like to thank HeeBong Yang and Rubayet Al Maruf for their time with fabrication and Paul Anderson and Sreesh for always lending a hand and tips in the lab .

Dedication

Table of Contents

List of Figures	viii
List of Tables	xii
1 Introduction	1
2 Hollow-Core Photonic Crystal Fiber	3
2.1 Conventional TIR Fibers	3
2.2 Photonic Crystal Bandgap	5
2.2.1 1D Photonic Bandgap	7
2.2.2 2D Photonic Bandgap	9
2.2.3 Bandgap Shift	13
3 Liquid-Filled HCPCF	14
3.1 Experimental Set-Up	14
3.1.1 Selective Filling	17
3.1.2 Full-Fiber Filling	20
3.2 Indocyanine Green	22
3.2.1 Experiment Set-Up	28
3.2.2 ICG in HCPCF	30
3.2.3 Particle-Mode Interaction and Optical Depth	34

4 Carbon Nanotubes	37
4.1 Characterizing Carbon Nanotubes	37
4.2 Nonlinear Optical Properties of CNTs	41
4.3 Fluorescence of CNTs	42
4.4 HCPCF Bandgap Overlap with CNT Excitation and Emission	45
4.4.1 Experiment Set-Up	47
5 Conclusion	50
References	52

List of Figures

2.1	Light propagation through optical fiber. The incident θ_i , reflected θ_r , and transmitted θ_t rays at the core-cladding boundary	3
2.2	(a)Cross-section a honey-comb HCPCF highlighting the PC pattern (b) Reduction of PC to 1-dimension (c)The 2-dimensional PC.	5
2.3	Band plot for a 1D photonic crystal with parameters-,-, solved using Finite Difference Time Domain(FDTD) method[6].	8
2.4	(a) primitive lattice vectors and (b) primitive reciprocal lattice vectors with first Brillouin zone (green) and irreducible Brillouin zone (red) depicted for a honeycomb lattice structure.	10
2.5	Band plot along the irreducible Brillouin zone for a honeycomb lattice with parameters $\varepsilon = 11, \frac{r}{a} = 0.34, a = 3.8\mu\text{m}$. Solved by using the Plane Wave Expansion(PWE) numerical method.	12
3.1	Fiber transmission experimental set-up. The path to the CCD camera is used to monitor the modeshape coming out of the fiber and the path to the spectrometer is used to measure the transmission spectrum of the fiber.	15
3.2	The transmission of heavy water(green) and regular water(blue) is shown for slabs of thickness ranging from 1cm to 8cm in increments of 1cm using absorption data by [11].	16
3.3	Side profile of collapsed cladding 1550HC fiber running the fiber splicer with varying current strength and duration.	17
3.4	Variation between fibers using splicer settings 70ms 25ms	18
3.5	Modeshape of 800 hollow-core fiber filled with (a)air (b)heavy water (c)DI water.	18

3.6	Transmission of H ₂ O and D ₂ O in a selectively-filled 800nm hollow-core fiber.	19
3.7	Modeshape of 1550 hollow-core fiber filled with (a)air (b)heavy water (c)DI water. Fiber filled with heavy water maintains a Gaussian profile while the fiber with regular distilled water shows some distortion.	20
3.8	Transmission of H ₂ O and D ₂ O in fully-filed and core-filled 1550nm hollow-core fiber.	21
3.9	(a) Depiction of the Homo-Lumo gap in organic semiconductors and the transition occurring between ground and excited states. (b) The chemical structure of ICG provided by MP Biomedicals.	22
3.10	Absorption cross-section at peak wavelengths 700nm(blue) and 780nm(green) for ICG dissolved in D ₂ O(a) and H ₂ O(b) . Data from [17] was fitted using a linear regression model.	23
3.11	Degradation of a 4.5ppm initial concentration sample after 4hrs of light exposure reduced to a 2ppm concentration.	26
3.12	(a)Fluoresce spectrum of 4.5ppm sample (b) Maximum fluorescence and maximum absorption spectrum of 4.5ppm initial concentration sample . . .	27
3.13	(a)Optical set-up to measuring output of the dye-filled fiber. The path to the CCD camera is used to monitor the modeshape coming out of the fiber. The path to the spectrometer (Case A) is used to measure the fluorescence spectrum and efficiency. The path to the photodiode (Case B) is used to measure the optical density of the fiber. (b)Optical set-up to measuring output of the dye in a 1cm cuvette. (c)Color and opacity difference between the stock solution (left) and diluted solution(right).	28
3.14	Absorption spectrum of ICG samples (a) 2.5 ppm concentration in core of 800nm HCPCF and (b) 4 ppm concentration in core an d cladding of 1550nm HCPCF.	30
3.15	(a) The maximum fraction of fluorescence is plotted against excitation wavelength for a 4ppm ICG sample in a 1cm piece of 1550nm HCPCF and 1cm cuvette. The maximum fraction of fluorescence of the ICG in the cuvette is only 4% of that measured in fiber. (b) The optical density at each excitation wavelength. The fraction of fluorescence spectrum of the 4ppm ICG solution in (c) 1550nm HCPCF (d) a cuvette.	32

3.16 Measurements of 3.7ppm ICG sample in a 2cm piece of core-filled 800nm HCPCF (a) The maximum fraction of fluorescence and optical density against excitation wavelength. (b) The fraction of fluorescence spectrum (c) Measured output peak power and fractional fluorescence as a function of input power.	33
3.17 (a)The number of molecules to create an optically dense medium as a function of average particle radius. Inset plot shows the dye concentration as a function of particle radius.(b) The rate increase in OD as the length of the fiber increases. For $OD = 1$: a sample concentration of 3.7ppm in 80nm HCPCF, $L_{fiber} = 2.28\text{cm}$ with a rate of $0.44(\frac{OD}{\text{cm}})$. For 1550nm HCPCF with a sample concentration of 4ppm. $L_{fiber} = 0.78\text{cm}$ with a rate of $1.27(\frac{OD}{\text{cm}})$	35
4.1 Chiralities of CNTs with red dots indicating metallic and blue dots semiconductors.	38
4.2 (a)The Kataura plot, showing the relationship between CNT diameter and energy separation. Red dots indicate metallic and black semiconducting. The density of states for (b) Metallic and (c) Semiconducting CNTs and their energy band gaps. The green line indicates the Fermi level. Plots generated using data from[40].	40
4.3 Group characteristics of CNTs colored by using variational parameters from[43], valid for diameters $> 0.5\text{nm}$. Color spectrum of plot denoting (a)chiral angle and (b)diameter. Increase in Stokes shifts with diameter along chiral difference ($n - m$) lines, noted in red and connected by black lines.	44
4.4 Hollow-core fiber bandgap overlayed on CNT emission vs. excitation wavelengths	46
4.5 Excitation/Emssion spectrum of CNTs falling within the D ₂ O-filled 1550HCPCF bandgap.	46
4.6 The experiential used set-up for measuring (a)Absorption and (c) Fluorescence of CNT samples in a cuvette. (b)The spectrum and intensity of the excitation beam at $\lambda = 645\text{nm}$ picked-offed the super continuum source. The power measures $48\mu\text{W}$ and fwhm= 6nm	48
4.7 (a) Absorbance spectrum of CNT sorted CNT sample (b)Absorbance of CNT sorted sample over 60 minutes, the absorbance of the sample stabilizes after 30 minutes.	49

- 5.1 Example NLECSL configurations integrating the liquid-HCPCF as the gain medium (a) Littrow configuration (b) Single-wavelength fiber-integrated approach with FBG 51

List of Tables

3.1	Absorption Cross Section parameter fitting of ICG dissolved in DI water. Fitting done with linear regression on σ vs. concentration data measured at $\lambda = 780nm$ from literature.	25
3.2	Absorption Cross Section parameter fitting of ICG dissolved in DI water. Fitting done with linear regression on σ vs. concentration data at $\lambda =$ $700nm$ from literature.	25
3.3	Absorption Cross Section parameter fitting of ICG dissolved in heavy water. Fitting done with linear regression on σ vs. concentration data at $\lambda =$ $700nm$ and $\lambda = 780nm$ from [17].	25
4.1	Thorlabs fiber bandgap shift. The ranges for HC1550 and HC800B are approximated from spectrum measurements and HC2000 and HC1060 are taken from NKT datasheets[53, 54].	45
4.2	CNTs with emission and excitation transmittable through HC1550 filled with D ₂ O.	46

Chapter 1

Introduction

With the latest developments in 1D and 2D materials, specialty optical waveguides, and fibers it has become possible to design robust small-scale nonlinear devices and sensors[32, 41] that are not burdened with taking up large amounts of space or constant realignment like traditional bulk-optical systems. Various waveguide platforms have been developed by exploring light-guidance and confinement. Liquid waveguides offer flexibility in tuning the intensity and spectrum filtering by filling them with liquids of various refractive-index and suspending dielectric or fluorescent particles in the liquid medium[31, 30, 29]. This opens the possibility to develop on-chip and fiber-integrated sensors and fluorescent light sources.

Hollow-core photonic crystal fibers (HCPCF) are able to confine light to an air core and offer a low-loss, high threshold powers, and tight confinement that isn't feasible in conventional optical fibers. Because of the hollow core, it is possible to fill such fibers with gas or laser-cooled atoms and produce strong light-matter interactions[12, 13] and provide a tool for building single-photon interaction and nonlinear systems. Some work also suggests that the optical bandgap and strong interactions are preserved in liquid-filled HCPCF [8] despite lower refractive-index contrasts. Combining the ideas of particle suspension in liquid waveguide sensors with the desirable mode-confinement of HCPCFs, this thesis explores the interaction of light with suspended fluorescent particles in liquid-filled HCPCFs.

The structure of this thesis is as follows. In Chapter 2 the theoretical background around fiber-optic waveguides using Total-Internal-Reflection (TIR) and Hollow-Core Photonic Crystal Fibers (HCPCF) is introduced. This is followed by the derivation of the bandgap-shift equation from the refractive-index scaling laws for HCPCF in low-index contrast regions, which provides the basis for predicting the bandgap of liquid-filled hollow-core

fibers. Chapter 3 details the filling procedure for core-filled HCPCF, which transforms the HCPCF to guide light via TIR like a conventional optical fiber, and completely liquid-filled HCPCF, which should follow the scaling laws. Experimental confirmation of the predicted band-gap shift and transmission losses are done for H₂O and D₂O as filling materials. Chapter 4 introduces the optical properties of Indocyanine Green (ICG), a fluorescent dye used to study light-matter interactions between the particles suspended in the liquid-core and the mode of the fiber. Following the results of ICG, the optical properties of carbon nanotubes(CNTs) are introduced in Chapter 5, developing an argument for CNTs as a promising fluorescing nano-particle to be used in liquid-fiber applications.

Chapter 2

Hollow-Core Photonic Crystal Fiber

2.1 Conventional TIR Fibers

Conventional optical fibers (and optical waveguides in general) are guided by TIR. Structurally, this is composed of a high refractive-index core n_2 surrounded by a lower refractive-index cladding n_1 , depicted in Fig.2.1. As light propagates through the the core, some light

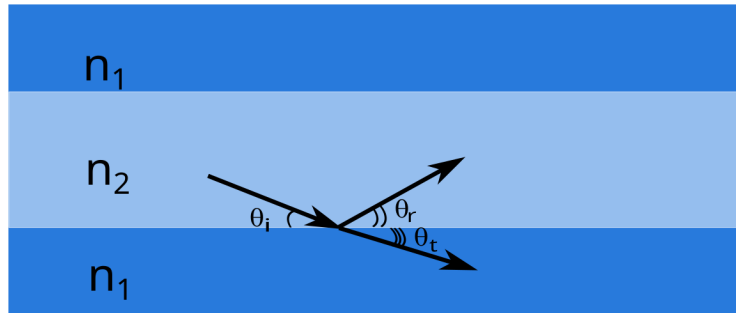


Figure 2.1: Light propagation through optical fiber. The incident θ_i , reflected θ_r , and transmitted θ_t rays at the core-cladding boundary

will be transmitted through the cladding while some is reflected back into the core. The relationship between the angles of incident and transmitted light is governed by Snell's Law:

$$n_1 \cos(\theta_i) = n_2 \cos(\theta_t) \quad (2.1)$$

If the refraction angle is at a minimum, then the light below a critical incident angle θ_c , will not propagate into the cladding and will only be reflected back into the core, hence "total

internal reflection”. From Snell’s law it is evident that the critical angle is dependent on the refractive-index contrast between the core and cladding,

$$\theta_c = \arccos(n_2/n_1) \quad (2.2)$$

and that for TIR-guided fibers the core refractive index must be higher than that of the cladding otherwise light will just be transmitted through the cladding, putting limitations on the minimum refractive-index of the core. Due to this limiting factor, TIR-guided fibers have limitations on the power transmission and loss due to propagation through the core material.

2.2 Photonic Crystal Bandgap

The refractive-index contrast constraints of traditional fibers are overcome by HCPCFs which are able to mitigate the propagation losses in the core by having a core of air, $n_{air} = 1$, the lowest possible refractive index. Light is instead trapped in the core by a photonic bandgap created by a surrounding photonic crystal cladding.

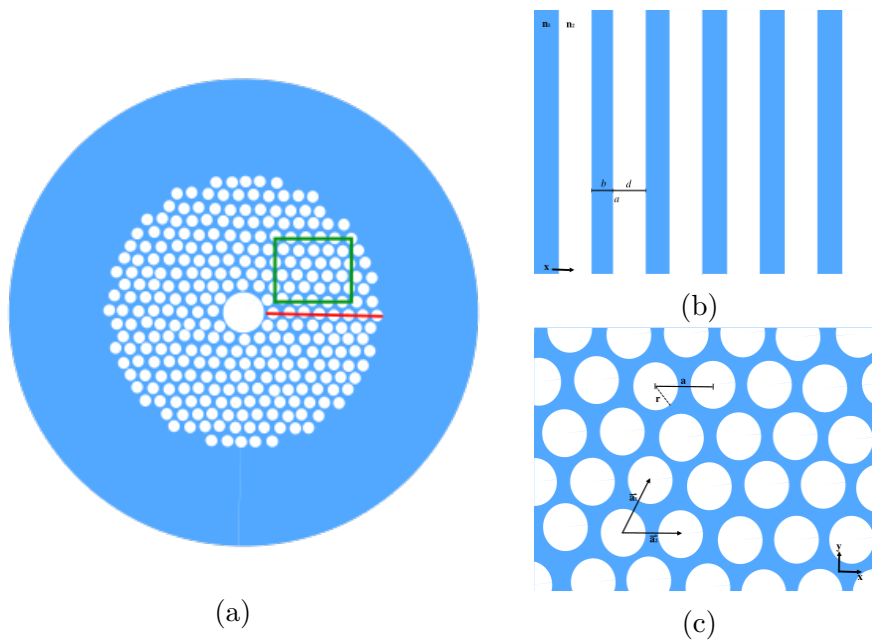


Figure 2.2: (a) Cross-section of a honeycomb HCPCF highlighting the PC pattern (b) Reduction of PC to 1-dimension (c) The 2-dimensional PC.

Photonic crystals consist of alternating refractive index in periodic structure, such as the 1D stack depicted in Fig.2.2(b) or 2D periodic array of air-holes seen in the HCPCF cross-section in Fig.2.2(c). A periodic non-magnetic medium will have repeating dielectric constant [1]

$$\varepsilon(\mathbf{r}) = \varepsilon(\mathbf{r} + \mathbf{a}) \quad (2.3)$$

Due to its discrete and invariant translational symmetry, the dielectric constant along the medium can be expanded as the Fourier series

$$\varepsilon(\mathbf{r}) = \sum_{\mathbf{G}} \varepsilon_{\mathbf{G}} e^{i\mathbf{G}\cdot\mathbf{r}} \quad (2.4)$$

where \mathbf{G} are the reciprocal lattice vectors such that $\mathbf{G} \cdot \mathbf{a} = 2\pi n$. The electric field can also be expressed as the Fourier integral

$$\mathbf{E}(\mathbf{r}) = \iiint d^3\mathbf{k} \mathbf{A}(\mathbf{k}) e^{i\mathbf{k}\cdot\mathbf{r}} \quad (2.5)$$

Using the Maxwell equations (2.6) the wave equation can be written in terms of the electric field

$$\begin{cases} \vec{\nabla} \times \vec{H} &= -i\omega\epsilon(\vec{r})\vec{E} \\ \vec{\nabla} \times \vec{E} &= i\omega\mu_0\vec{H} \end{cases} \quad (2.6)$$

$$\nabla \times (\nabla \times \mathbf{E}) - \omega^2 \varepsilon(\mathbf{r}) \mu_0 \mathbf{E} = 0 \quad (2.7)$$

Substituting (2.4) and (2.5) into the above equation results in the dispersion relation:

$$\mathbf{k} \times (\mathbf{k} \times \mathbf{A}(\mathbf{k})) + \omega^2 \mu_0 \sum_{\mathbf{G}} \varepsilon_{\mathbf{G}} \mathbf{A}(\mathbf{k} - \mathbf{G}) = 0 \quad (2.8)$$

in which for any vector \mathbf{K} the solutions of (2.8) for the coefficient $\mathbf{A}(\mathbf{K})$ are grouped with the coefficients $\mathbf{A}(\mathbf{K} - \mathbf{G})$, decoupling the coefficients of other vectors that cannot be expressed in the form $\mathbf{K} - \mathbf{G}$. Disregarding the decoupled vectors, the total electric field can be described as a superposition of normal modes with regard to a chosen vector \mathbf{K} :

$$\mathbf{E}_{\mathbf{k}}(\mathbf{r}) = \sum_{\mathbf{G}} \mathbf{A}(\mathbf{K} - \mathbf{G}) e^{i(\mathbf{k}-\mathbf{G}) \cdot \mathbf{r}} \quad (2.9)$$

The Bloch theorem for the electric field can be pulled out from (2.9)

$$\mathbf{E}_{\mathbf{k}}(\mathbf{r} + \mathbf{a}) = e^{i\mathbf{k}\cdot\mathbf{a}} \mathbf{E}_{\mathbf{k}}(\mathbf{r}) \quad (2.10)$$

$$\mathbf{u}_k(\mathbf{r}) = \sum_{\mathbf{G}} \varepsilon_{\mathbf{G}} e^{i\mathbf{G}\cdot\mathbf{r}} \quad (2.11)$$

$$\varepsilon_{\mathbf{G}} = \frac{1}{V} \int d^3\mathbf{r} e^{-i\mathbf{G}\cdot\mathbf{r}} \mathbf{u}_k(\mathbf{r}) \quad (2.12)$$

Returning to (2.8), can fix ω to find the corresponding \mathbf{K} and normal modes os the system. However, in the case of photonic crystals there are ranges of frequencies that have no \mathbf{K} 's with real solutions, which implies that waves of these frequencies cannot propagate through the photonic crystal. These non-propagating frequencies are referred to as the photonic band gap.

2.2.1 1D Photonic Bandgap

1D photonic bandgap structure models for hollow-core optical fibers [3] demonstrate the core idea of bandgap fibers. In one dimension, the periodicity of dielectric constant is described by $\varepsilon(z) = \varepsilon(z + a)$ where $a = b + d$, the length of one period. The reciprocal lattice vector will be $\mathbf{G}_n = n \frac{2\pi}{a} \hat{z}$ and plugging into the Fourier series expansion of $\varepsilon(z)$ from (2.4)

$$\varepsilon(z) = \sum_{n=-\infty}^{\infty} \varepsilon_n e^{in \frac{2\pi}{a} \hat{z}} \quad (2.13)$$

From the reduction to propagation in the z-direction with the electric field oriented in x-direction, (2.8) simplifies to

$$K^2 A(K) + \omega^2 \mu_0 \sum_{n=-i\infty}^{\infty} \varepsilon_n A(K - n \frac{2\pi}{a}) = 0 \quad (2.14)$$

Expanding the Fourier coefficients to the 1st order and reducing the equations to the dominant coefficients of the form $A(K)$ and $A(K - \frac{2\pi}{a})$. $|K - g| = K$ and $K = \frac{\pi}{a}$ gives a system of equations that can be solved to find the dispersion relation $\omega(K)$.

$$\begin{cases} (K^2 - \omega^2 \mu_0 \varepsilon_{00}) A(K) = \omega^2 \mu_0 \varepsilon_1 A(K - g) \\ \omega^2 \mu_0 \varepsilon_{-1} A(K) = ((K - g)^2 - \omega^2 \mu_0 \varepsilon_{00}) A(K - g) \end{cases} \quad (2.15)$$

The equations relating these two modes have a solution at

$$(K^2 - \omega^2 \mu_0 \varepsilon_{00}) ((K - g)^2 - \omega^2 \mu_0 \varepsilon_{00}) - (\omega^2 \mu_0 \varepsilon_1) (\omega^2 \mu_0 \varepsilon_{-1}) = 0 \quad (2.16)$$

Noting that $\varepsilon_1 = \varepsilon_{-1}^*$ and $K \approx 2g$ simplifies the relationship to

$$\omega_{\pm}^2 = \frac{K^2}{\mu_0(\varepsilon_{00} \mp |\varepsilon_1|)} \quad (2.17)$$

The dispersion relation has two possible solutions, which specify the top and bottom of the photonic bandgap edges, as illustrated in Fig.2.3.

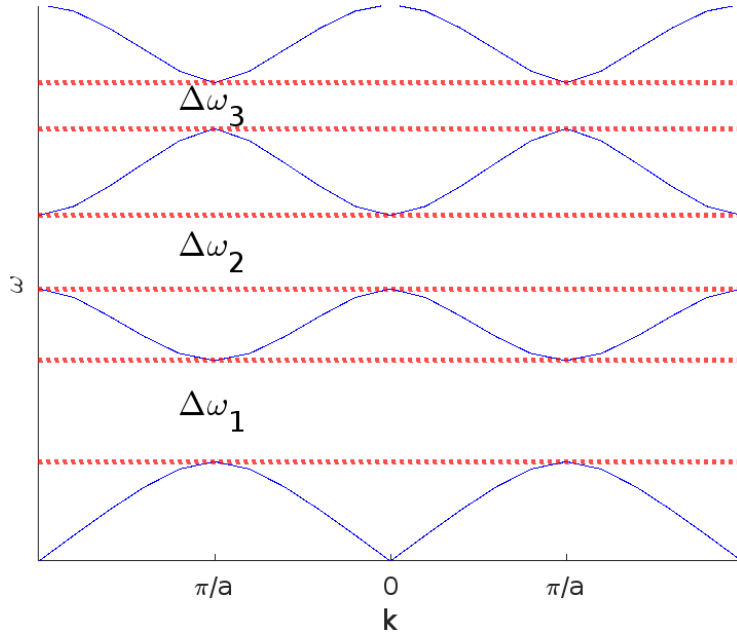


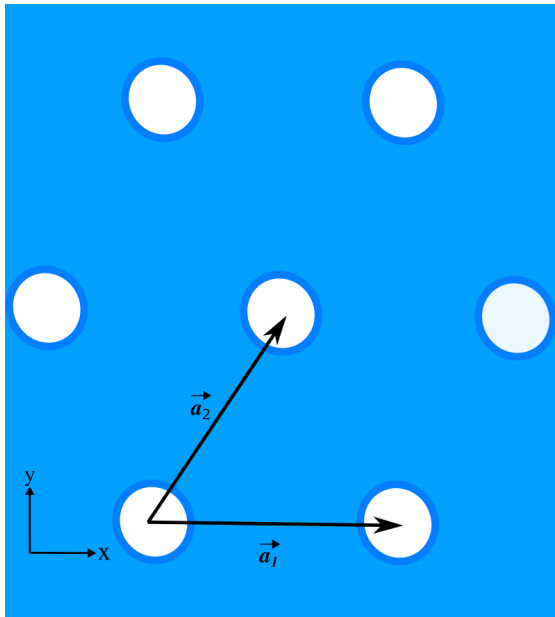
Figure 2.3: Band plot for a 1D photonic crystal with parameters-, -, solved using Finite Difference Time Domain(FDTD) method[6].

If solving for the wavevector at a frequency between the two roots ω_{\pm} , only complex solutions will exist. This means that only evanescent waves, not electromagnetic waves, propagate through the medium while the electromagnetic waves are reflected back; the medium acts as a mirror for the bandgap wavelengths.

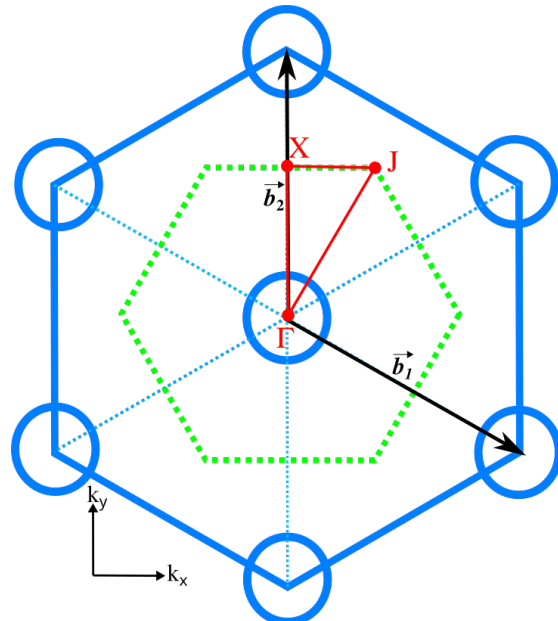
This is the phenomenon that allows for HCPCF to guide certain frequencies of light: wavelengths in the bandgap are reflected by surrounding Bragg Grating confining them to the core of the fiber, while the rest are allowed to propagate through the grating.

2.2.2 2D Photonic Bandgap

To understand the full picture of light propagation in hollow-core fiber, the expansion to the 2D case pictured in Fig.2.2c is needed. However, with the electromagnetic waves now propagating in two dimension there is an added layer of complexity with the TE TM wave polarizations and the bandgaps. In addition to controlling the refractive index of the material and the period of the lattice, the lattice structure and hole radius will affect the performance of the photonic crystal, the latter playing a large role in the completeness of the photonic bandgap. In the 2D photonic crystal, the in-plane guided modes will have either magnetic fields in-plane and electric fields perpendicular to the lattice (TE modes), or electric fields in-plane and magnetic fields perpendicular to the lattice (TM modes). As the TE and TM modes are perpendicular to each other they may exhibit wildly different dispersion relations, which means that an optical bandgap is not guaranteed to persist for all polarizations[2]. This is certainly the case for square lattice phonic crystals, but other patterns such as the honeycomb (which is the structure in our HCPCF) have a bandgap persisting for all polarizations[4]. It is important to consider all polarization effects when making decisions about photonic crystal patterns for two or more dimensions.



(a)



(b)

Figure 2.4: (a) primitive lattice vectors and (b) primitive reciprocal lattice vectors with first Brillouin zone (green) and irreducible Brillouin zone (red) depicted for a honeycomb lattice structure.

Considering the lattice structure in Fig.2.4(a) and taking propagation in the xy-plane ($K_z = 0$ and $z = 0$ for simplicity), the wavevector and position vectors reduce to $\mathbf{K}_{||} = k_x \hat{x} + k_y \hat{y}$ and $\mathbf{r}_{||} = x \hat{x} + y \hat{y}$. The primitive lattice vectors of a honeycomb photonic crystal will be:

$$\mathbf{a}_1 = a \hat{x} \quad \mathbf{a}_2 = \frac{a}{2} \hat{x} + \frac{a\sqrt{3}}{2} \hat{y} \quad (2.18)$$

and transforming to the momentum-space, $\mathbf{b} \cdot \mathbf{a} = 2\pi\delta_{ij}$, as shown in Fig.2.4(b) the primitive reciprocal lattice vectors are

$$\mathbf{b}_1 = \frac{2\pi}{a} \hat{x} - \frac{2\pi}{a\sqrt{3}} \hat{y} \quad \mathbf{b}_2 = \frac{4\pi}{a\sqrt{3}} \hat{y} \quad (2.19)$$

Taking these in combination of n, m integer scaling factors, the reciprocal lattice vector is defined $\mathbf{G}_{||} = n\mathbf{b}_1 + m\mathbf{b}_2$. The electromagnetic field defined for a two dimensional system is

$$\mathbf{E}(\mathbf{r}) = e^{i\mathbf{k} \cdot \mathbf{r}} \sum_{m=-\infty}^{\infty} \sum_{n=-\infty}^{\infty} \mathbf{E}_{m,n} e^{i(n\mathbf{b}_1 + m\mathbf{b}_2) \cdot \mathbf{r}} \quad (2.20)$$

and the correlating Fourier expansion of dielectric function (2.12)

$$\varepsilon_{\mathbf{G}_{||}} = \frac{1}{a' \cdot b'} \int dx dy e^{i(G_x x + G_y y)} \mathbf{u}_k(x, y) \quad (2.21)$$

are substituted into (2.6). By utilizing the lattice symmetry and periodicity, the problem can be restricted to only solve for Bloch modes inside the of the irreducible Brillouin zone. The first Brillouin zone is defined by the perpendicular bisectors to the primitive reciprocal lattice vectors, depicted in green in Fig.2.4(b) and can be further subdivided into the irreducible Brillouin zone shown in red. In order to find the photonic bandgap, solving the dispersion equation just along the irreducible Brillouin zone is sufficient. For a honeycomb lattice, the k -path to follow would be

$$\begin{cases} |\Gamma X| = \frac{2\pi}{a\sqrt{3}}, & k_x = 0, 0 < k_y < \frac{2\pi}{\sqrt{3}a} \\ |X J| = \frac{2\pi}{3a}, & 0 < k_x < \frac{2\pi}{3a}, k_y = \frac{2\pi}{\sqrt{3}a} \\ |\Gamma J| = \frac{4\pi}{3a}, & 0 < k_x < \frac{2\pi}{3a}, k_y = \sqrt{3}k_x \end{cases} \quad (2.22)$$

Discretizing (2.20) and (2.21) then picking a few points along the k -path, numerical methods can be used to solve for the optical bandgap. Fig.2.5 shows the resulting TE bandgap for a honeycomb lattice with parameters $\varepsilon = 11$, $\frac{r}{a} = 0.34$, $a = 3.8\mu\text{m}$ using Plane Wave Expansion(PWE)[6].

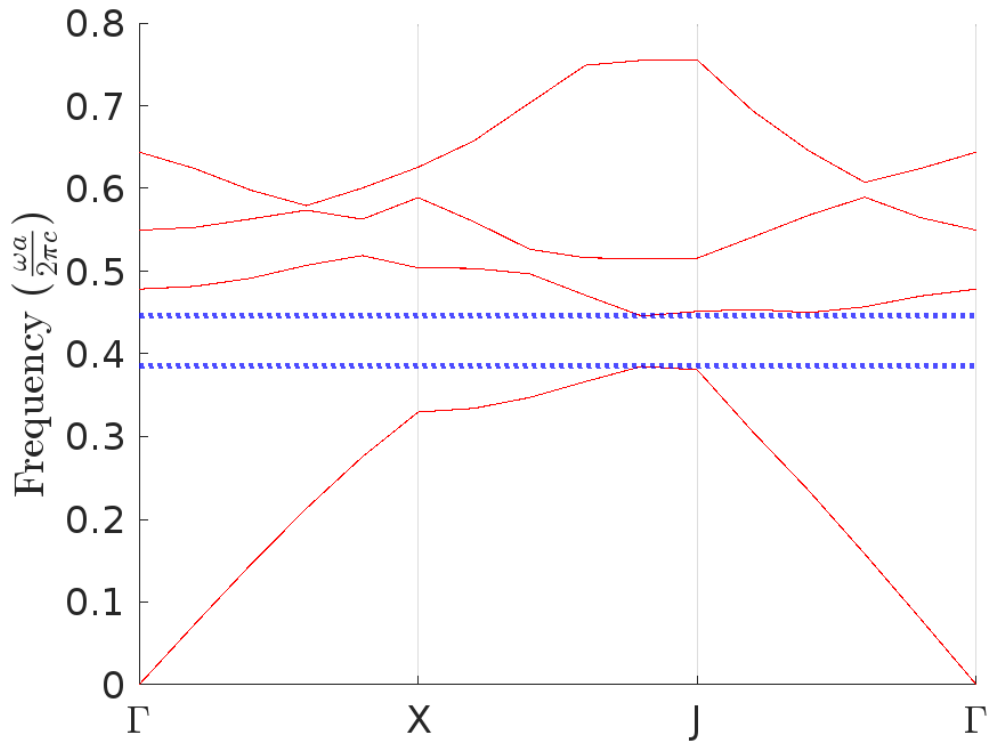


Figure 2.5: Band plot along the irreducible Brillouin zone for a honeycomb lattice with parameters $\varepsilon = 11$, $\frac{r}{a} = 0.34$, $a = 3.8\mu\text{m}$. Solved by using the Plane Wave Expansion(PWE) numerical method.

2.2.3 Bandgap Shift

The position of the HCPCF bandgap is dependent on the periodicity refractive-index and changing the material within the photonic crystal will cause a change in the bandgap. Though a small index contrast in the a periodic medium is assumed in the derivation, the bandgap shift has been experimentally confirmed to still hold under high contrasts[8]. The scalar wave equation for a given periodic medium will maintain the same bandgap structure but scaling the wavelength proportionately in compensation[7]. The scaling law for the wave equation for the transverse coordinates $X = x\Lambda^{-1}$ $Y = y\Lambda^{-1}$ where Λ is a solution to the transverse scale.

$$n(X, Y) = \begin{cases} 1, & n_1 \text{ (high RI)} \\ 0, & n_2 \text{ (low RI)} \end{cases} \quad (2.23)$$

and factors into the normalized scaled wave equation:

$$\nabla_{\perp}^2 \Psi + (v^2 n(X, Y) - w^2) \Psi = 0 \quad (2.24)$$

With $\nabla_{\perp} = \partial^2 / \partial X^2 + \partial^2 / \partial Y^2$ solving for the frequency parameter v^2 and eigenvalue w^2 :

$$\begin{aligned} v^2 &= \Lambda^2 k^2 (n_1^2 - n_2^2) \\ w^2 &= \Lambda^2 (\beta^2 - k^2 n_2^2) \end{aligned} \quad (2.25)$$

From the equation above it is evident that the eigenvalue is determined by the frequency parameter and the index distribution function $n(X, Y)$. This implies that w^2 and v^2 are invariant with changes to the parameters $k = \omega/c$, Λ , n_1 , n_2 . In the HCPCF case where the glass refractive index is held constant and the air in the fiber is replaced by a new material. The equations can be rewritten with $n_1 = n_{glass}$ and $n_2 = n_{air} = 1$:

$$\begin{aligned} v^2 - w^2 &= \Lambda^2 (k^2 n_{glass} - \beta^2) \\ v &= k \Lambda n_{glass} \sqrt{n_{air} - \frac{n_{air}}{n_{new}}} \end{aligned} \quad (2.26)$$

The initial index contrast $N_0 = \frac{n_{air}}{n_{glass}}$ moves to $N = \frac{n_{new}}{n_{glass}}$ with the change in RI $n_{air} < n_{new} < n_{glass}$. This leads to the new center bandgap to be governed by the equation:

$$\lambda = \lambda_0 \sqrt{\frac{1 - N^{-2}}{1 - N_0^{-2}}} \quad (2.27)$$

Chapter 3

Liquid-Filled HCPCF

In this chapter follows a background on different filling methods, the integrity of the scaling laws, and transmission of liquid-filled HCPCF.

3.1 Experimental Set-Up

For the transmission measurements, shown in Fig.3.1, fibers were cut to be between 6cm and 8cm in length. To ensure consistent coupling and positioning, light was coupled to the core of the fiber by connecting to a solid-core PM780HP fiber via a mechanical splicing chip [9].

In our experiments two different filling methods are tested: full fiber filling, and selective filling, as well as two filling liquids: deionized water (which will be referred to as DI Water or H_2O) and heavy water D_2O . Fibers that are fully-filled with water will produce a frequency shift in the bandgap. On the other hand, when the core is selectively filled with water, the core refractive index will be greater than effective refractive index of the cladding and light will be guided via total-internal reflection. H_2O , while widely available and a common solvent, has high absorption loss in the near infrared (NIR) but its most common isotope D_2O has comparatively much less absorption loss in the same region (Fig.3.2). The transmission in HCPCF are explored for H_2O for its ubiquity while D_2O for its suitability as a filling liquid in the NIR.

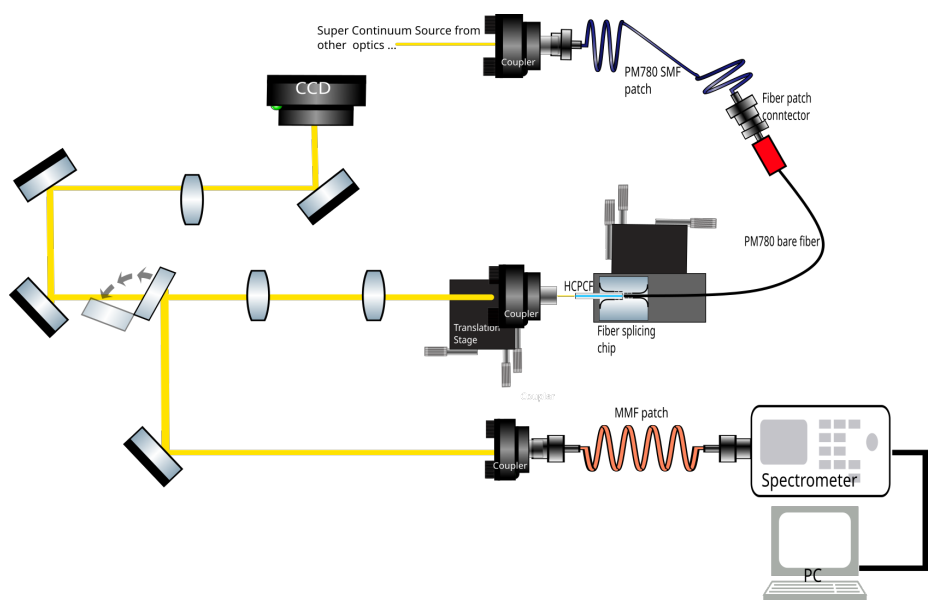


Figure 3.1: Fiber transmission experimental set-up. The path to the CCD camera is used to monitor the modeshape coming out of the fiber and the path to the spectrometer is used to measure the transmission spectrum of the fiber.

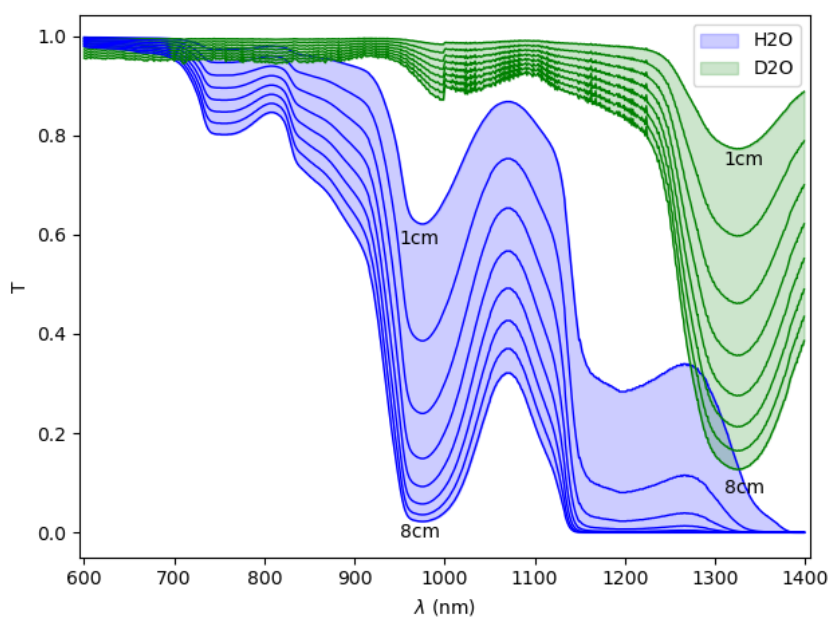


Figure 3.2: The transmission of heavy water(green) and regular water(blue) is shown for slabs of thickness ranging from 1cm to 8cm in increments of 1cm using absorption data by [11].

3.1.1 Selective Filling

Filling Method

To selectively fill the core of 800nm HCPCF, the photonic crystal cladding was collapsed while leaving the hollow-core open and is similarly filled with liquid using capillary action. The cladding is collapsed by placing the HCPCF opposite of a solid-core fiber in a fusion splicer [10] and adjusting arc current duration and power to melt the cladding structure while remaining distanced enough to prevent fusion with the solid-core fiber.

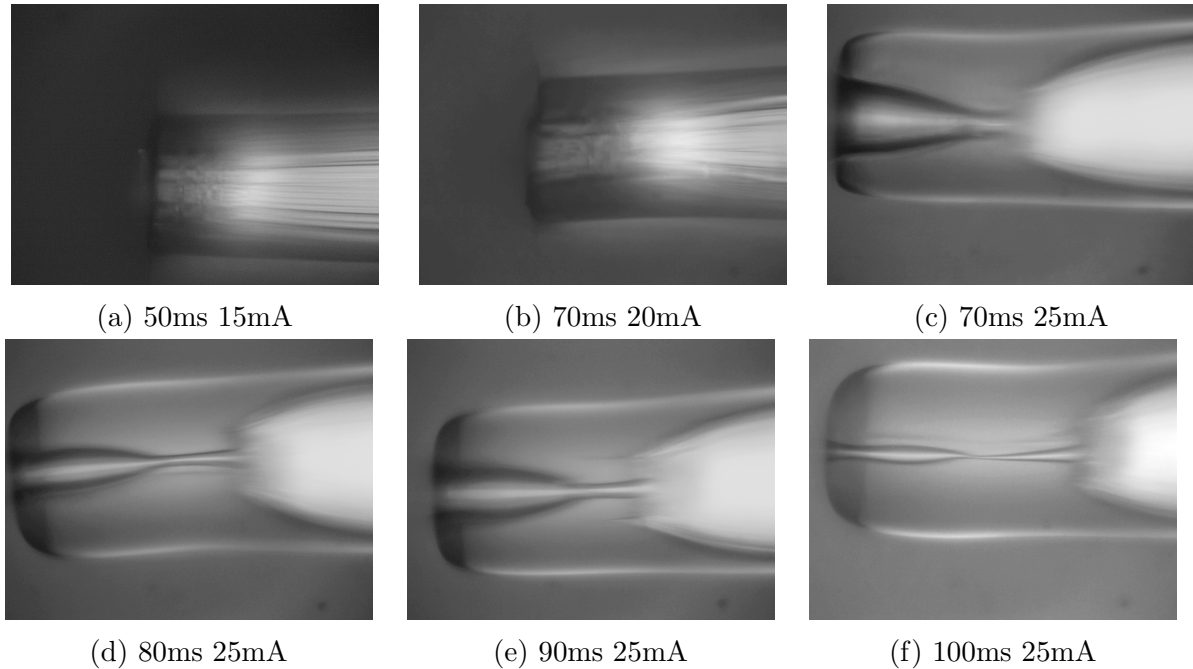


Figure 3.3: Side profile of collapsed cladding 1550HC fiber running the fiber splicer with varying current strength and duration.

In Fig.3.3 the extent of collapse of the cladding is compared to various timing and power for an ORIENTEK T40 fusion splicer. The optimal setting is around an arc power of 25mA for a 70ms duration, though due to the imprecision in the arc power discharge the cladding on occasion will be overexposed, as shown in Fig.3.4.

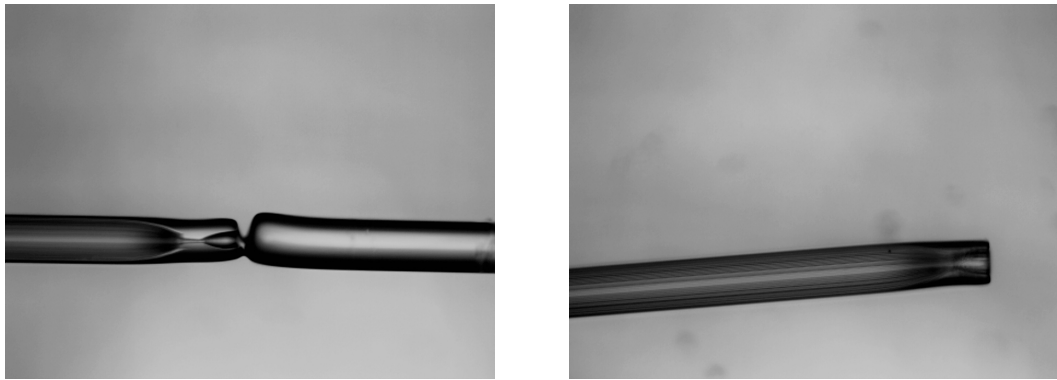


Figure 3.4: Variation between fibers using splicer settings 70ms 25ms

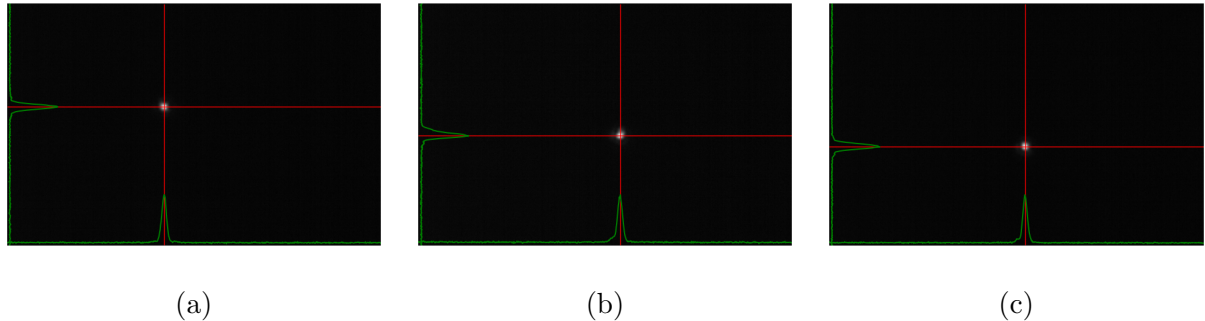


Figure 3.5: Modeshape of 800 hollow-core fiber filled with (a)air (b)heavy water (c)DI water.

Transmission

The air-filled 800nm HCPCF covers a transmission spectral range of 750nm–950nm. Light exits the fiber with a Gaussian mode shape, as shown in Fig.3.5. In a H_2O core, the coupling efficiency of the fiber drops to 31%, while a heavy water filled core is less affected by absorption over this region and retains a coupling efficiency of up to 67%.

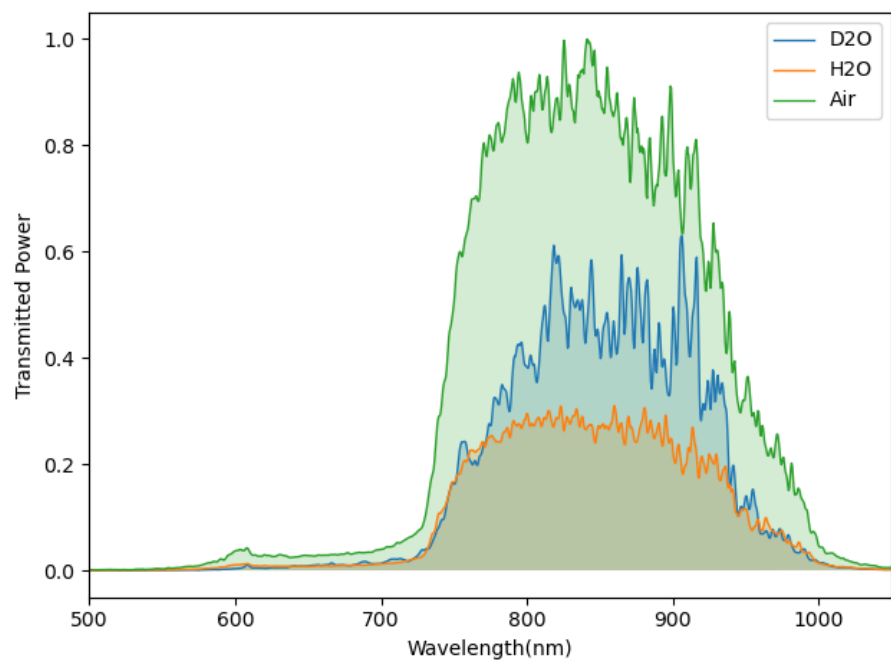


Figure 3.6: Transmission of H₂O and D₂O in a selectively-filled 800nm hollow-core fiber.

3.1.2 Full-Fiber Filling

Filling Method

The air in 1550nm HCPCF was replaced with deionized water and heavy water by utilizing capillary action.

Transmission

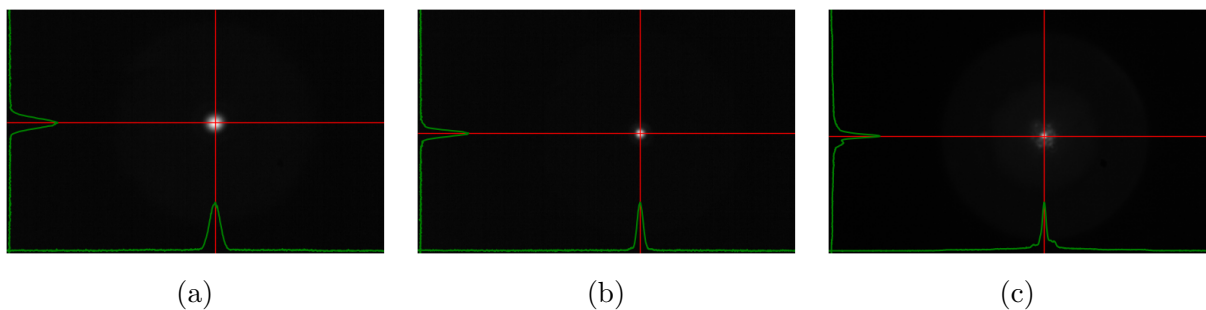


Figure 3.7: Modeshape of 1550 hollow-core fiber filled with (a)air (b)heavy water (c)DI water. Fiber filled with heavy water maintains a Gaussian profile while the fiber with regular distilled water shows some distortion.

The air-filled 1550nm HCPCF covers a transmission spectral range of 1200nm–1700nm. With a filled core and cladding, the spectral range shifts to transmitting wavelengths between 600nm–1100nm for both heavy water and water, confirming the scaling laws. Heavy water achieved a coupling efficiency of 47%, but water only 16%. While the D₂O fiber modeshape retains a Gaussian profile, the H₂O mode shape contains noise as some light also leaks from the photonic structure. The absorption effects of H₂O severely reduce the transmission for wavelengths above 820nm, while compares well to the transmission of the D₂O fiber below 820nm and could arguably be used as a filling liquid.

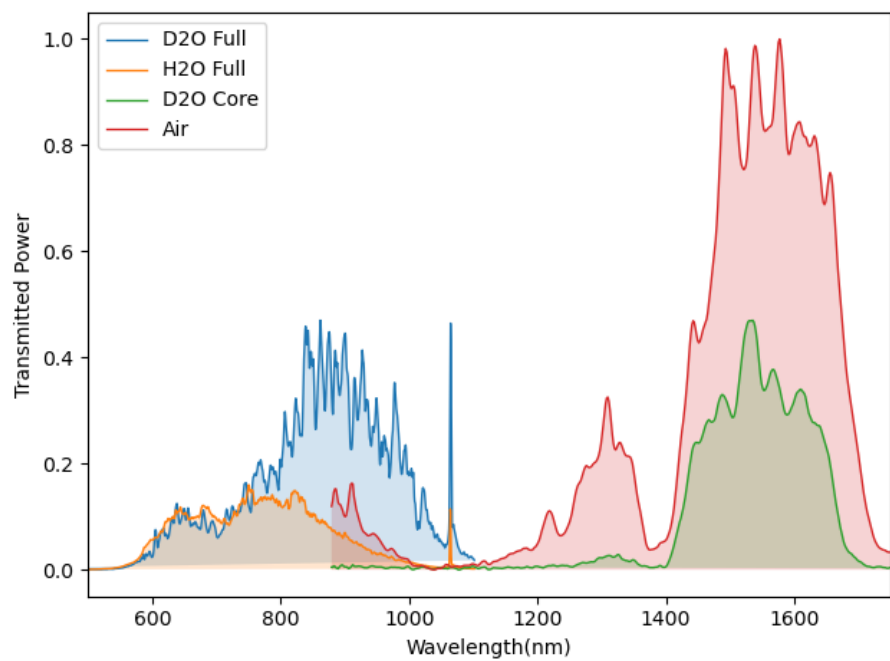


Figure 3.8: Transmission of H_2O and D_2O in fully-filled and core-filled 1550nm hollow-core fiber.

3.2 Indocyanine Green

Indocyanine green (ICG) - a fluorescent dye often used in microscopy imaging[23, 24] - was dissolved in water and put into HCPCF due to its excitation and emission wavelength overlap with the bandgap of fully-filled 1550nm and core-filled 800nm HCFCP. This particular dye is an organic semiconductor with Homo-Lumo gap calculations estimating a 2eV energy gap, with variations depending on the solvent[16]. The HOMO and LUMO energy levels in organic semiconductors are parallel to the maximum valence and minimum conduction, and the aforementioned energy gap falls within the range of energy bandgaps found in inorganic semiconductors.

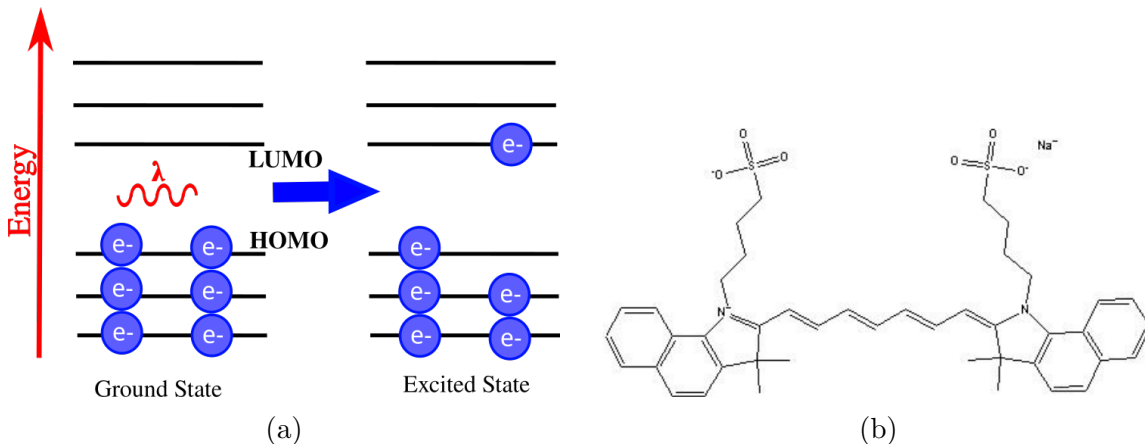


Figure 3.9: (a) Depiction of the Homo-Lumo gap in organic semiconductors and the transition occurring between ground and excited states. (b) The chemical structure of ICG provided by MP Biomedicals.

The following section details the the optical properties of ICG and measurements of the optical properties when confined in HCPCF.

Absorption Cross-Section

ICG absorbs wavelengths between 600-900nm. The absorption is largely bimodal, with the greatest excitation occurring at 780nm and 700nm, but transforms into a monomeric distribution at 780nm at low concentrations and 700nm at high concentrations.

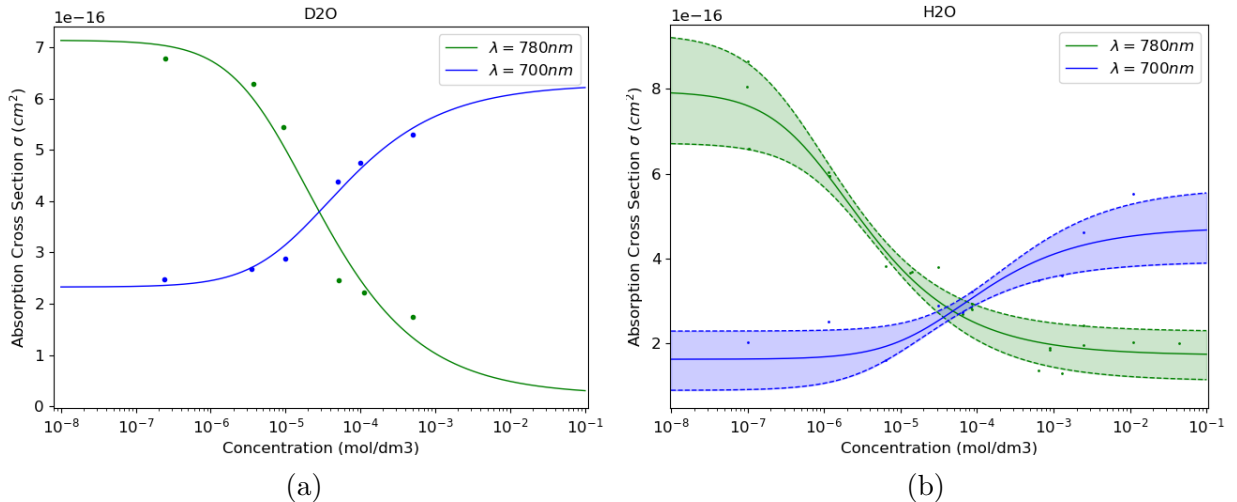


Figure 3.10: Absorption cross-section at peak wavelengths 700nm(blue) and 780nm(green) for ICG dissolved in D₂O(a) and H₂O(b) . Data from [17] was fitted using a linear regression model.

Due to the chemical formation of ICG, the absorption of the molecule when dissolved in a solvent is highly concentration-dependent. ICG is made up of monomers, which are a type of molecule that can react with other monomers to form polymer chains. In the case of ICG, its monomers react with each other to form dimers, a chain of two joint monomers. With higher concentrations monomers are closer to each other, causing the molecules to have an increased likelihood to shift from monomers to dimers, which in turn are less likely to be excited and shift the center absorption wavelength. The concentration of monomers M to dimers D is governed by the equilibrium reaction:



and law of mass action relation concentration

$$[D] = K_D[M]^2 \quad (3.2)$$

where K_D is the dimerization constant. Written in terms of concentration C and mole fractions, $[M] = x_M C = (1 - x_D)C$ and $[D] = \frac{x_D}{2}C$, the mole fraction of dimers can be written in terms of the dimerization constant and concentration.

$$x_D = 1 + \frac{1}{4K_D C} - \sqrt{\left(1 + \frac{1}{4K_D C}\right)^2 - 1} \quad (3.3)$$

The absorption cross-section model for ICG[19, 21] will be an average of the effects of the monomers and dimers, where σ_M and σ_D are the monomer and dimer absorption cross-sections respectively.

$$\sigma = x_M \sigma_M + x_D \sigma_D = \sigma_M - x_D (\sigma_M - \sigma_D) \quad (3.4)$$

Plugging (3.3) into (3.4), remaining parameters can be found by doing a linear regression fit to absorption cross-section vs. concentration data from literature. The expected absorption cross-section can be calculated for any concentration. For ICG dissolved in H₂O, the existing literature presents some variation and so the upper/lower bounds and average were taken, while data for ICG dissolved in D₂O was based on [17]. The behavior in H₂O and D₂O are quite similar and are plotted in Fig.3.10. At lower concentrations the absorption cross-section is slightly greater for D₂O than H₂O, with the reverse for high concentrations.

$\lambda_{peak} = 780nm$	K_D	σ_M	σ_D
[17]	6.01×10^5	9.29×10^{-16}	2.28×10^{-16}
[18]	1.03×10^5	6.74×10^{-16}	1.54×10^{-16}
[19]	1.40×10^5	6.72×10^{-16}	1.11×10^{-16}
Average	3.06×10^6	7.94×10^{-16}	1.72×10^{-16}

Table 3.1: Absorption Cross Section parameter fitting of ICG dissolved in DI water. Fitting done with linear regression on σ vs. concentration data measured at $\lambda = 780nm$ from literature.

$\lambda_{peak} = 700nm$	K_D	σ_M	σ_D
[17]	3.00×10^3	2.29×10^{-16}	25.68×10^{-16}
[19]	3.06×10^4	8.89×10^{-16}	3.93×10^{-16}
Average	9.31×10^3	1.62×10^{-16}	4.74×10^{-16}

Table 3.2: Absorption Cross Section parameter fitting of ICG dissolved in DI water. Fitting done with linear regression on σ vs. concentration data at $\lambda = 700nm$ from literature.

λ_{peak}	K_D	σ_M	σ_D
780nm	3.22×10^4	7.14×10^{-16}	2.68×10^{-17}
700nm	1.67×10^4	2.833×10^{-16}	6.28×10^{-16}

Table 3.3: Absorption Cross Section parameter fitting of ICG dissolved in heavy water. Fitting done with linear regression on σ vs. concentration data at $\lambda = 700nm$ and $\lambda = 780nm$ from [17].

Photostability

At high concentrations, ICG behaves as a “J-aggregate”, a category of dyes that shift in the absorption band to larger wavelengths in certain solvents. When mixed into water and other solvents, ICG shifts over time to a center wavelength of 893nm. This process can be accelerated under high heat. In high-concentration forms (in the range of 1000ppm solutions) [20], J-aggregates can be stored at room temperature for several months. However, in such a state the dye will be too optically dense to observe any optical excitation and when diluted to perform such measurements, the J-aggregates will begin to detach into smaller molecules within 24hrs. The effects of dye concentration on storage life in aqueous solutions becomes a tricky balance at single-digit ppm concentrations. At that concentration, the fluorescence intensity of the dye is at its greatest but it degrades to undetectable levels in just a couple of hours under optimal storage conditions[18, 22]. The rate of deterioration occurs linearly based on the initial concentration of ICG[17], but the amount of light exposure of the solution will also exasperate the degradation rate[22].

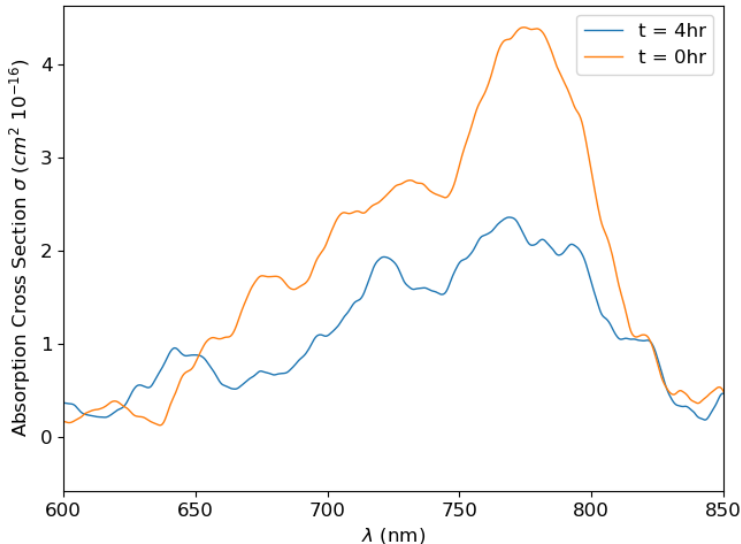


Figure 3.11: Degradation of a 4.5ppm initial concentration sample after 4hrs of light exposure reduced to a 2ppm concentration.

Fluorescence

Photoluminescence in the dye is observed in the range of 750-900nm, therefore overlapping with the absorption spectrum. The peak emission wavelength for ICG varies within 800nm-820nm[21, 22] when excited at 780nm, and decreases as solution concentration increases. The dimerization effects are attributed to (a) the formation of weakly fluorescent ICG molecular aggregates at high concentrations (b) self-quenching and (c) re-absorption of the emitted fluorescence by the ICG molecules due to overlap of the absorption and emission spectra. In the J-aggregate form the excitation wavelength shifts to 834nm and the emission peaks at 890nm although low quantum yield and strong light scattering does not lend to accurate measurements[20].

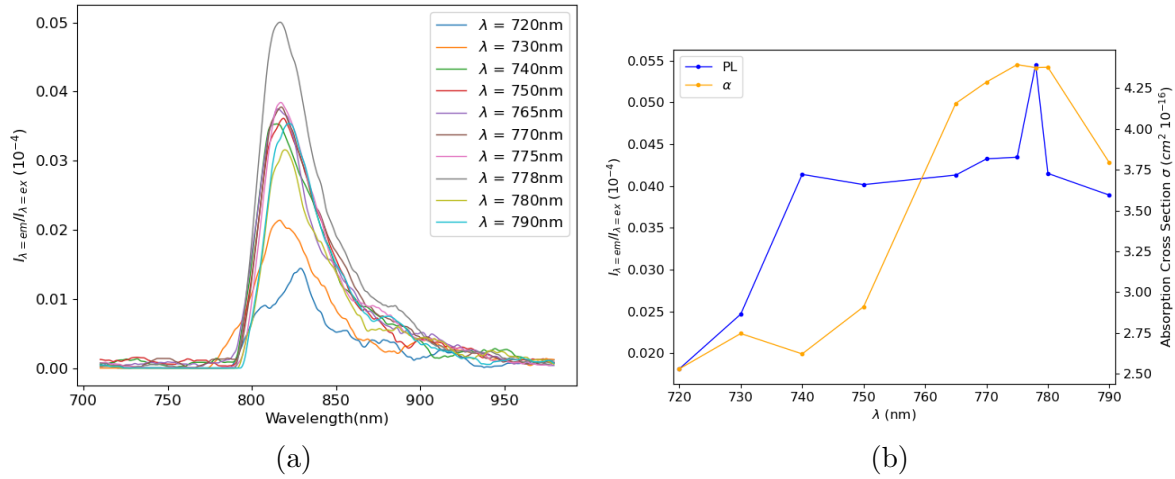


Figure 3.12: (a) Fluorescence spectrum of 4.5 ppm sample (b) Maximum fluorescence and maximum absorption spectrum of 4.5 ppm initial concentration sample

3.2.1 Experiment Set-Up

The experimental set-up for the dye-filled HCPCF is very similar to that of the previously introduced HCPCF set-up, but includes a few additions. A fiber beam splitter was added between the fiber patch coming from the laser coupler and the bare fiber to monitor input power and wavelength. For fluorescence detection out of the fiber, a front-face fluorescence collection scheme was used and a long pass filter was placed in the path in order to filter out the incident light from the fluorescence. Additionally, a fiber clamp was placed on a translation stage to control the position and angle at which the bare fiber is positioned in the mechanical splicer chip. Due to tolerance issues in the mechanical splitter chips made for 1550nm HCPCF. The prior development of these chips done by lab members of NPQO[9] tuned the fabrication recipe for coupling between $130\mu\text{m}$ to $125\mu\text{m}$ diameter fibers, specifically measuring the coupling between 800nm HCPCF to PM780HP fibers, resulting in a production of chips highly consistent in diameter. The 1550nm HCPCF however, has a diameter of $120\mu\text{m}$. Mechanical splicer chips of $120\mu\text{m}$ to $125\mu\text{m}$ diameter fibers are fabricated along with the $130\mu\text{m}$ to $125\mu\text{m}$, but they are not of consistent quality and the majority of chips are over-exposed leading to the fibers to be loose and not level with each other in the chip. This resulted in average coupling rates of $> 10\%$ if supported by the chip structure only.

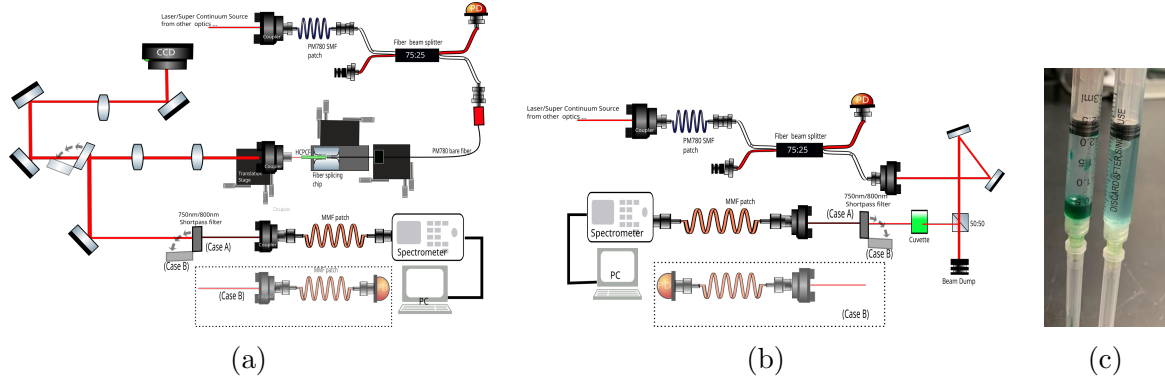


Figure 3.13: (a)Optical set-up to measuring output of the dye-filled fiber. The path to the CCD camera is used to monitor the modeshape coming out of the fiber. The path to the spectrometer (Case A) is used to measure the fluorescence spectrum and efficiency. The path to the photodiode (Case B) is used to measure the optical density of the fiber. (b)Optical set-up to measuring output of the dye in a 1cm cuvette. (c)Color and opacity difference between the stock solution (left) and diluted solution(right).

Sample Preparation

ICG powder was purchased from MP Biomedicals in quantities of 5mg per vial. A stock solution was made by dissolving 5mg of powder in 5mL of H₂O, then a low-concentration solution is made by diluting 10 μ L of stock solution into 2.5mL of either D₂O/H₂O. In a second approximate method for making low-concentration solutions, the tip of a syringe needle was used to scoop up a small amount of dye and then dissolve it in 5-10mL of D₂O/H₂O, working by eye based on the hue and opacity of the dye sample (See Fig.3.13(c)). The absorption of the sample was then measured in a cuvette and fitted to the concentration-based absorption cross-section data to find the concentration of the sample.

3.2.2 ICG in HCPCF

Low-concentration samples of dye were prepared and used it to fill a 800nm HCPCF core and 1550nm HCPCF core and cladding. The measured absorption cross-section of the dye, shown in Fig.3.14, presents additional absorption effects caused by the fiber, notably the narrower bandgap of the 800nm HCPCF. Additionally, there is an observed 18nm shift in the peak absorption from 778nm to 796nm in the 1550nm bandgap-shifted liquid-filled fiber, while the 800nm liquid-core fiber has an insignificant 4nm shift in peak from 775nm to 771nm.

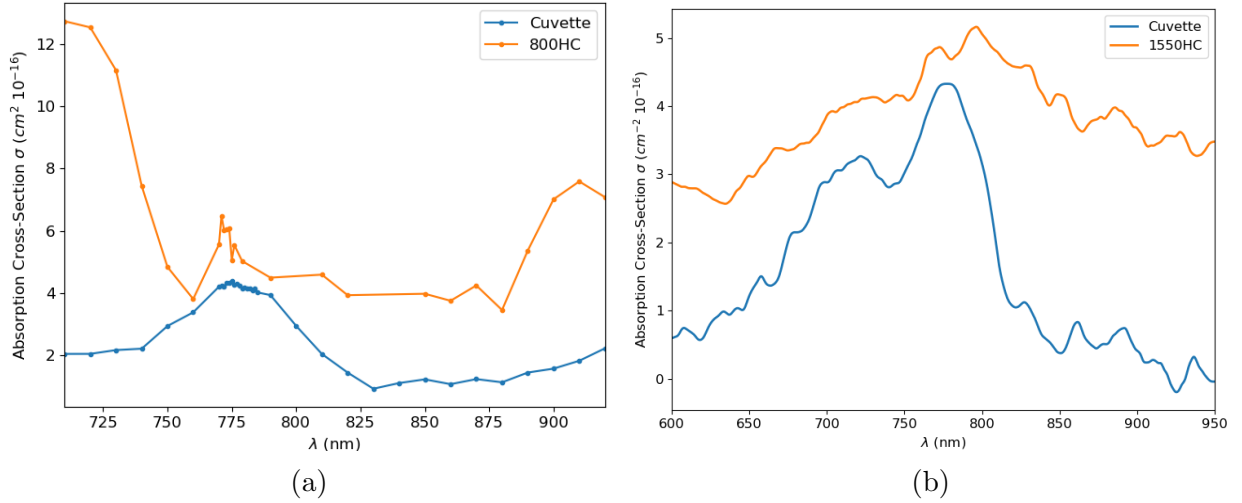


Figure 3.14: Absorption spectrum of ICG samples (a) 2.5 ppm concentration in core of 800nm HCPCF and (b) 4 ppm concentration in core and cladding of 1550nm HCPCF.

For 800nm core-filled HCPCF, ICG solutions were prepared with H_2O and D_2O solvents, but fluorescence was only guided in the D_2O . In the 800HC fiber there was already significant loss coming from the narrow bandgap in combination with lower refractive index contrast of using a liquid medium, as half of the absorption spectrum is outside the bandgap; The absorption of effects of H_2O in the NIR (discussed in chapter 2) and re-absorption from the overlapping excitation-emission spectra is suspected to be greater than the number of emitted photons. The fluorescence guided in the 800nm HCPCF was also influenced by the bandgap, shown in Fig.3.16b. The emission had a large shifts in peak for excitation between 745 – 775nm - wavelengths at the edge of the bandgap and

with high absorption effects - varying peak fluorescence between 800 and 820nm while for excitation above 775nm the fluorescence stayed centered at 805nm.

Fluorescence was also in ICG-filled 1550nm HCPCF with D₂O as solvent, which had the best ratio of fluorescence intensity to emission intensity (“fraction of fluorescence”). For a 4ppm ICG sample the fraction of fluorescence are compared in Fig.3.15 for excitation wavelengths below the emission wavelength range. The peak fluorescence in the cuvette was at 820nm, but was shifted down 10nm to 810nm in the fiber and the fraction of fluorescence in 1550nm HCPCF was ~ 35x greater than that measured through the cuvette. For the 3.7ppm sample in core-filled 800nm HCPCF similar fraction of fluorescence to the cuvette sample were measured at the excitation wavelength of peak absorption(778nm).

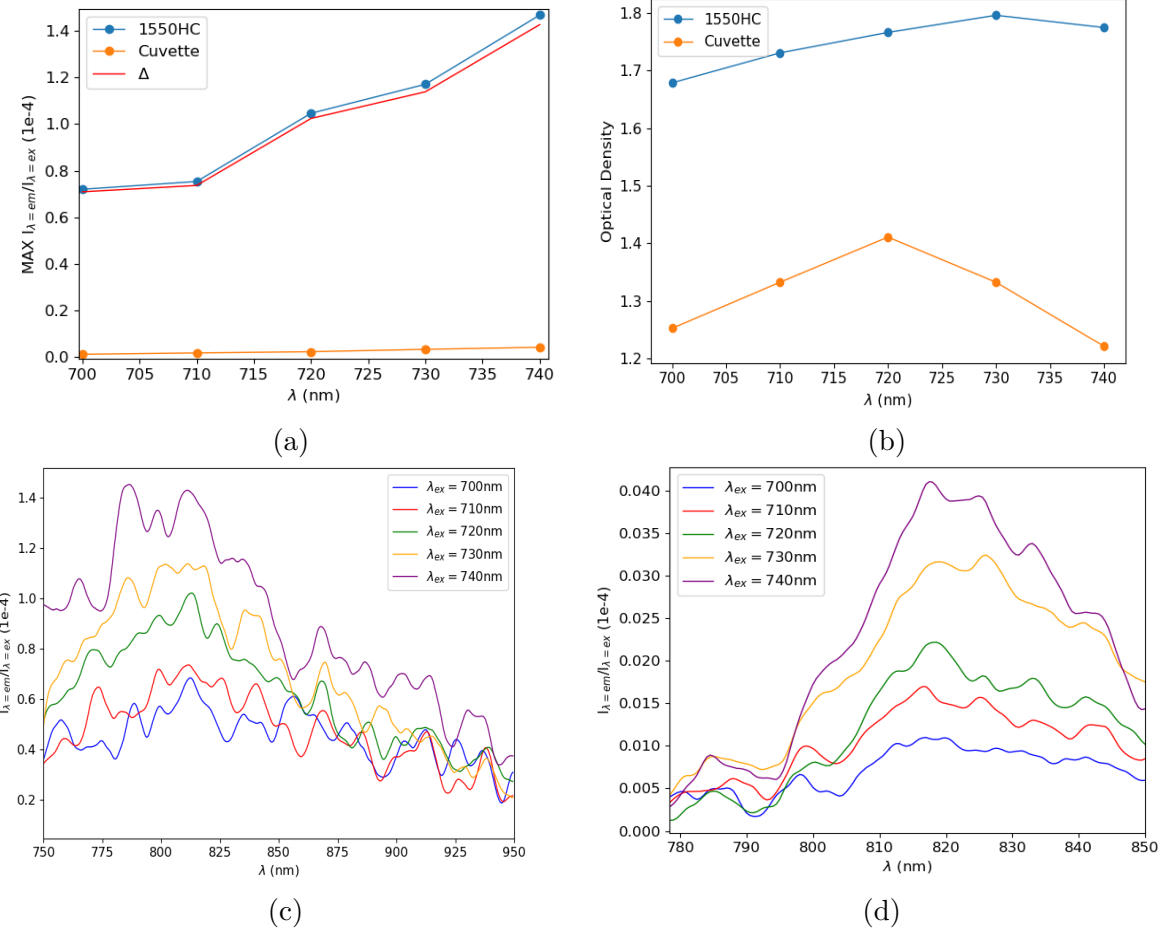


Figure 3.15: (a) The maximum fraction of fluorescence is plotted against excitation wavelength for a 4ppm ICG sample in a 1cm piece of 1550nm HCPCF and 1cm cuvette. The maximum fraction of fluorescence of the ICG in the cuvette is only 4% of that measured in fiber. (b) The optical density at each excitation wavelength. The fraction of fluorescence spectrum of the 4ppm ICG solution in (c) 1550nm HCPCF (d) a cuvette.

At the maximum absorption wavelength, the fraction of fluorescence and output power at the excitation wavelength are measured as a function of the input power, shown in Fig.3.16c. The fraction of fluorescence peaks at an input power of $50\mu W$, while the output power increases logarithmically and appears to approaching a limit on the transmission. Overall, the fluorescence efficiency is of 0.00051% in the 800nm HCPCF $\lambda_{ex} = 778$ and for 1550nm HCPCF 0.014% at $\lambda_{ex} = 740$ nm, which is comparable to other optofluidic waveguides [29]. *||||||| Stashed changes*

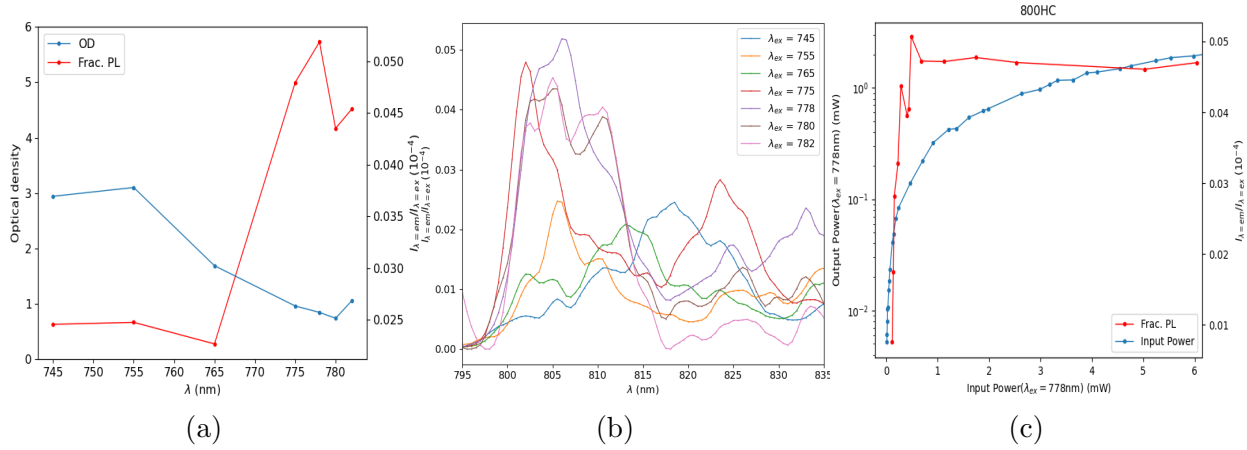


Figure 3.16: Measurements of 3.7ppm ICG sample in a 2cm piece of core-filled 800nm HCPCF (a) The maximum fraction of fluorescence and optical density against excitation wavelength. (b) The fraction of fluorescence spectrum (c) Measured output peak power and fractional fluorescence as a function of input power.

3.2.3 Particle-Mode Interaction and Optical Depth

Optical depth (OD) is a measurement of the opacity of a system, related to the transmitted intensity by $T = \exp(-OD)$. With particles distributed throughout the fiber, the interaction between the beam and particles inside the fiber needs to be taken into account. When considering a single particle interacting with the mode function of a waveguide the strength of the particle interaction will depend on its position within the mode[14, 15]. The effective mode area of the waveguide is then relevant only in relation to the position of the particle.

$$\sigma_M = \frac{\int dx dy |f_k(x, y)|^2}{|f_k(x_p, y_p)|^2} \quad (3.5)$$

where $f_k(x, y)$ is the transverse mode function and $f(x_p, y_p)$ is the position of the particle. In the case of a Gaussian mode function (as would be in a HCPCF), the photon interaction with the particle will be stronger in the center of the mode and weak at the edges. The optical depth (OD) for a single particle the ratio of the scattering cross-section to that of the effective mode-area $OD = \frac{\sigma_0}{\sigma_M}$, so to find the optical depth over the entire ensemble the product of the number density of the sample and optical depth of each emitter is integrated over the volume :

$$OD_{fiber} = \int_0^{L'} \int_0^{r'} n(r, z) OD(2\pi r) dr dz \quad (3.6)$$

where r' and L' represent the radius and length of the ensemble. When the fibers are fully liquid cladding and core, due to the low interaction and guidance of photons in the PC structure, an approximation is made constricting the mode function strictly to the core. This simplifies the dimensions of the integration to just be the radius and length of the fiber. This assumes that the particulates outside of the core do not have a significant contribution. If the distribution of molecules is taken to be uniform along the fiber length and radius of the core, then the number density is:

$$n(r, z) = \frac{N_{particle}}{V_{fiber}} = \frac{N_{particle}}{\pi r_{core}^2 L_{fiber}} \quad (3.7)$$

The integral will simplify to

$$\begin{aligned} OD_{fiber} &= \int_0^{L_{fiber}} \int_0^{r_{core}} n(r_{core}, L_{fiber}) \sigma_0 \frac{2}{\pi w_0^2} e^{-\frac{2r^2}{w_0^2}} (2\pi r) dr dz \\ &= N_{particle} \frac{\sigma_0}{\pi r_{core}^2} \left(1 - e^{-\frac{2r_{core}^2}{w_0^2}} \right) \end{aligned} \quad (3.8)$$

Optical Density Calculations for ICG

For ICG dispersed in water, molecule aggregate radii have been measured between $2\text{nm} - 200\text{nm}$ [25], with J-aggregates forming at radii $> 50\text{nm}$ [26]. Due to the low concentration samples of dye used in our experiments, the lower range of molecule diameter is expected, meeting the Raleigh scattering approximation condition $\frac{2\pi r}{\lambda} \ll 1$, the scattering cross-section is

$$\sigma_0 = \frac{2\pi^5(2r_{particle})^6}{3\lambda^4} \left(\frac{N^2 - 1}{N^2 + 2} \right)^2 \quad (3.9)$$

where $N = \frac{n_{particle}}{n_{solvent}}$. After applying the parameters above and (3.9) to (3.8), the estimated concentration of ICG molecules for optically dense medium ($OD_{fiber} = 1$) has a range of $N_{particle} = 1.5 \times 10^8 \sim 2.0 \times 10^{14}$ molecules and $N_{particle} = 8.2 \times 10^7 \sim 1.1 \times 10^{14}$ molecules for 1550nm and 800nm HCPCF respectively varying the ICG aggregate radii within the approximation condition.

For calculations of optical density with ICG molecules in the 1550nm HCPCF, the core

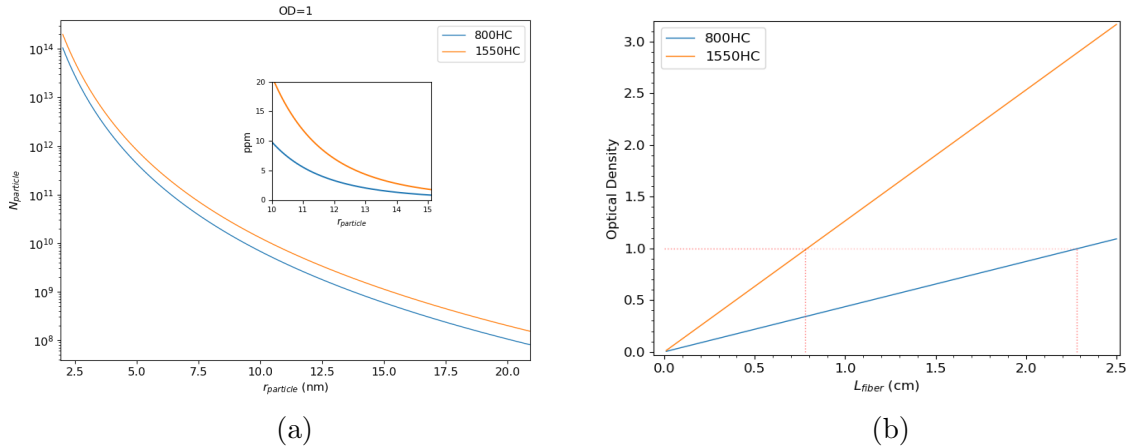


Figure 3.17: (a) The number of molecules to create an optically dense medium as a function of average particle radius. Inset plot shows the dye concentration as a function of particle radius. (b) The rate increase in OD as the length of the fiber increases. For $OD = 1$: a sample concentration of 3.7ppm in 80nm HCPCF, $L_{fiber} = 2.28\text{cm}$ with a rate of $0.44(\frac{OD}{cm})$. For 1550nm HCPCF with a sample concentration of 4ppm. $L_{fiber} = 0.78\text{cm}$ with a rate of $1.27(\frac{OD}{cm})$

radius is taken as $r_{core} = 5 \pm 0.05\mu\text{m}$ with beam waist $w_0 = 4.5 \pm 0.05\mu\text{m}$. For this $L_{fiber} = 1\text{cm}$ piece of fiber, the number of molecules contained in a perfectly filled core is

expected to be

$$N_{particle} = M_{ICG} * C * V_{fiber} = \frac{1mol}{774.98g} * \frac{4mg}{1dm^3} * \pi(5\mu m)^2(1cm) = 2.441 \times 10^9 molecules \quad (3.10)$$

Using the measured optical density in the fiber, Fig.3.15b the estimated radius of the aggregate ICG molecules is $r_{particle} = 13.7 \pm 0.2nm$. Carrying out the same calculations for the $L_{fiber} = 2cm$ 800nm HCPCF, the number of molecules contained in a perfectly filled core will be $N_{particle} = 2.54 \times 10^9$. The fiber has a core radius $r_{core} = 3.75 \pm 0.05\mu m$ with beam waist $w_0 = 2.75 \pm 0.05$ and using the measured optical density in the fiber, Fig.3.16a, the estimated radius of the aggregate ICG molecules is $r_{particle} = 11.5 \pm 0.26nm$. These molecule radii are well in agreement, but since the 800nm HCPCF ICG solution is a slightly lower concentration, the average $r_{particle}$ is expected to form slightly smaller aggregates.

Chapter 4

Carbon Nanotubes

First discovered by S.Iijima and T. Ichihashi in 1993, carbon nanotubes (CNTs) are single layers of graphene rolled up into a hollow cylinder near 1nm in diameter and average near 1 μm in length. Due to the extreme diameter to length ratio, their geometry allows them to be treated as a 1D material. CNTs possess unique optical properties that have found a wide range of applications[35], the most of importance to us is the lack of photobleaching and the fact that they do not degrade in water, the main permanence issues with using fluorescent dyes like ICG. In this section follows a description of the attributes that make them attractive from an optical standpoint, first going over their characterizing properties then nonlinear optical properties and fluorescence.

4.1 Characterizing Carbon Nanotubes

The main descriptive property of CNTs is the chiral vector, the inter-valued scaling of the unit vectors for the honeycomb structure of graphene, written in the form (n, m).

$$C_h = na_1 + ma_2 = (n, m) \quad (4.1)$$

The unit vectors describing the lattice are of equal length and in Cartesian coordinates are defined

$$a_1 = \left(\frac{\sqrt{3}}{2}, \frac{1}{2}\right)\sqrt{3}a_{C-C}a_2 = \left(\frac{\sqrt{3}}{2}, -\frac{1}{2}\right)\sqrt{3}a_{C-C} \quad (4.2)$$

where a_{C-C} is the length of the carbon bond. For graphene, $a_{C-C}=1.421$ (\AA) but for CNTs is approximately 1.44(\AA) with variation coming from the tube curvature[39]. From

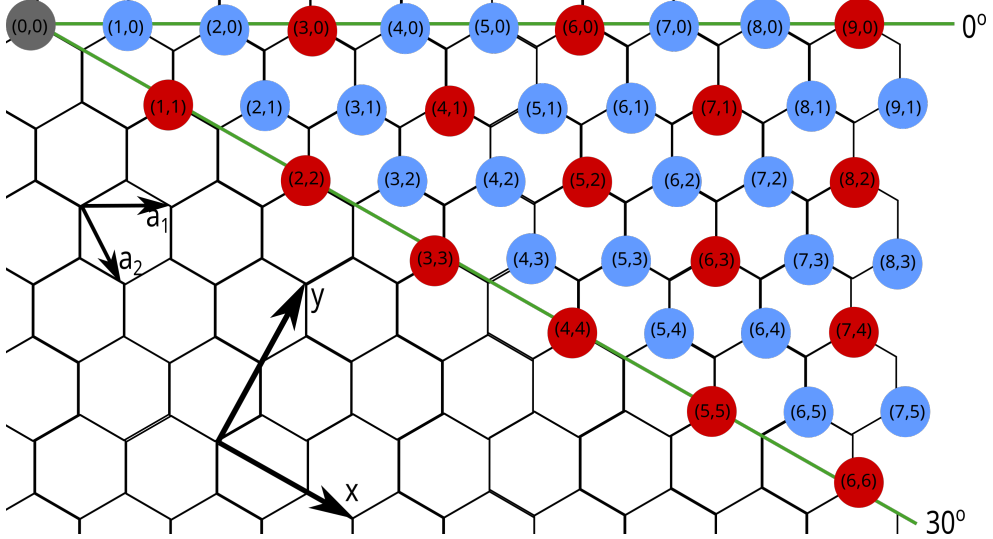


Figure 4.1: Chiralities of CNTs with red dots indicating metallic and blue dots semiconductors.

the chiral vector, much about the electronic and optical properties of individual CNTs can be inferred. The angle between the unit vectors, known as the chiral angle θ , gives the direction of the chiral vector and the diameter, d_t , of the CNT are related to the chiral numbers:

$$\theta = \tan^{-1} \left[\frac{m\sqrt{3}}{m + 2n} \right] \quad (4.3)$$

$$d_t = \frac{a_{CC}\sqrt{3}}{\pi} \sqrt{n^2 + nm + m^2} \quad (4.4)$$

The chiral angle is typically defined between 0° (a "zigzag" configuration) and 30° (an "armchair" configuration), labeled in Fig.4.1 due to the six-fold rotational symmetry lattice, as CNTs of mirrored chiral angles will have the sample opto-electrical properties.

As can be seen from the above definition, the tube diameter of CNTs is quantized. This quantization stems from the additional electron confinement around their circumference

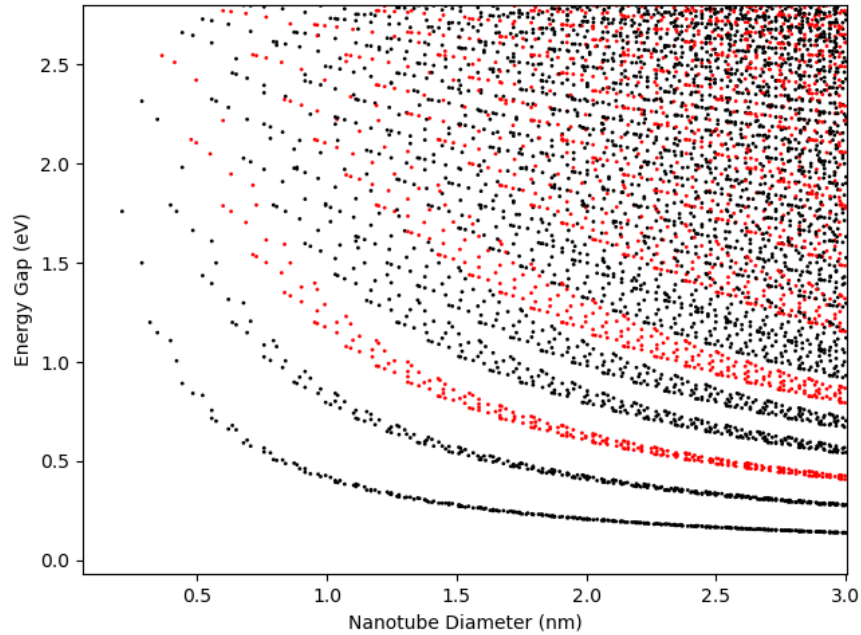
$$C_h \cdot \kappa = 2\pi q \quad (4.5)$$

as the cutting joining of the edges of graphene form the tubes only occurs at lines intersecting the lattice vertices. κ , the cutting line along the graphene energy bands, at integer value q positions forms a the corresponding pattern of metallic or a semiconductors

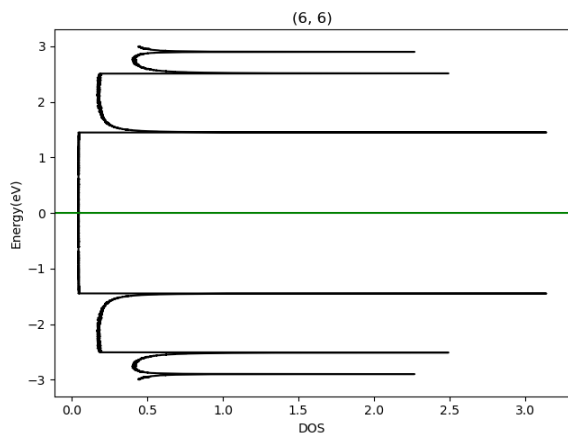
[33] with all CNTs with a difference in chiral numbers $|m - n|$ that are multiples of 3 emerging as metallic. Work by H. Kataura et. al [38] first plotted the energy differences between the van Hoven transitions, corresponding to the peaks in the conduction and valence bands enumerated starting from the Fermi energy, indicated in the 1D DOS plots in Fig.4.2(b)(c) later determined from [39]. The relationship of the first van Hoven transition to the diameter is found to be

$$E_{11} = \frac{2\gamma a_{C-C}}{d} \quad (4.6)$$

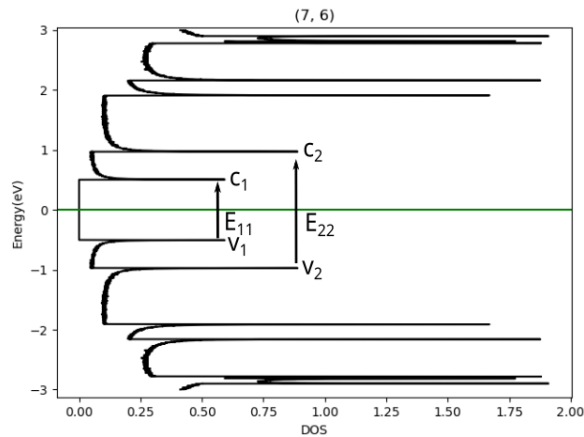
is shown in Fig.4.2(a), with the average band gap energies split along semiconductor and metallic chiral values. The absorption peak wavelength of a nanotube sample is determined by the mean tube diameter, and the absorption spectral bandwidth will be determined by the tube diameter distribution of the CNT sample.



(a)



(b)



(c)

Figure 4.2: (a)The Kataura plot, showing the relationship between CNT diameter and energy separation. Red dots indicate metallic and black semiconducting. The density of states for (b) Metallic and (c) Semiconducting CNTs and their energy band gaps. The green line indicates the Fermi level. Plots generated using data from[40].

Polarization Dependence

Single isolated CNTs exhibit polarization dependence with the electric field in optical selection rules, i.e. the possible transitions from one quantum state to another [37]. Polarization dependence is only strong in zigzag-type nanotubes, the parity of the dipole operator (-1 in the horizontal plane dipole operator along the z-axis and +1 in the x-y plane) thus indicates absorption of light with the optical polarization parallel to the axial direction of the tube. However, in a bundle or random-oriented CNT grouping there will be no polarization dependence and it is not something that is of concern in CNTs dispersed in a solution.

4.2 Nonlinear Optical Properties of CNTs

The general relationship between the polarization and electric field of a material is defined [35] as

$$P(t) = \epsilon_0(\chi^{(1)}E(t) + \chi^{(2)}E^2(t) + \chi^{(3)}E^3(t) + \dots) \quad (4.7)$$

where $\chi^{(1)}$ is the linear susceptibility and $\chi^{(2)}$ and $\chi^{(3)}$ are the second and third order susceptibility. Due to symmetry of the CNT's structure, the second-order susceptibility is zero but a large third-order nonlinearity in CNTs has been measured [46] and is theorized to be a product of the one dimensional motion of the delocalized π -band electrons at a fixed lattice ion configuration [47]. The third-order nonlinearity is responsible for the saturable absorption α of a material as well as the nonlinear Kerr effect. The refractive index for such a material will be composed of the real part of the third-order susceptibility with I defining the optical intensity, n_0 as the linear refractive index, n_2 and n is the nonlinear refractive index.

$$n = n_0 + n_2I = n_0 + \frac{3Re[\chi^{(3)}]}{4\epsilon_0cn_0^2}I \quad (4.8)$$

Saturable absorption is a phenomenon where high intensity light will reduce the absorption of a material, but at weak intensity, the light will be absorbed and cause attenuation. This property of materials with strong third-order susceptibility like CNTs can be used to filter out weaker optical signals in noisy optical pulses, while simultaneously allowing strong pulses to pass through. The absorption coefficient is composed of the imaginary part of the third-order susceptibility and α_0 , α_{int} , and ω are the linear absorption coefficient, the

non saturable absorption coefficient, and optical angular frequency respectively:

$$\begin{aligned}\alpha &= \frac{\alpha_0}{1 + \frac{I}{I_s}} + \alpha_{int} \\ &\sim \alpha_0 + \alpha_{int} + \frac{3\omega Im[\chi^3]}{2\epsilon_0 c^2 n_0^2} I\end{aligned}\tag{4.9}$$

the saturation intensity I_s is the power per unit area it takes in a steady state to reduce the absorption to half of completely saturated value, referred to as the unbleached state. Saturable absorption is observed in all materials with optical absorption resulting from electron transition between two energy levels [37], but it is rare to find materials that have a recovery time that has a fast recovery time compared to the pulse duration. In bundles of CNTs with a variety of diameter sizes, entanglement between semiconducting and metallic via electrons tunneling and coupling from semiconducting CNTs to metallic CNTs [42] can result in picosecond to femtosecond range recovery time. Bundled CNTs have found application in ultra-fast laser applications where this sort of recovery time is needed, having been successful implemented in mode-locking femtosecond fiber-lasers[49, 50, 51, 52].

4.3 Fluorescence of CNTs

Arriving at the interest in CNTs for this thesis, semiconducting CNTs can be optically excited and emit fluorescence[55] when well-dispersed. Bundled CNTs or placed on a substrate have little to no fluorescence at all, as interactions between CNTs cause increased quenching effects, the highest fluorescence quantum yields are seen in CNTs suspended in aqueous solutions. Though certain solvents mix better with certain chiralities CNTs to increase fluorescence, isolation to single chiralities one of the largest factors in increasing fluorescence. Desired type of CNTs can be targeted and isolated in a single step using modified aqueous two-phase extraction(ATPS)[48].In this process, hydration modulating agents are mixed in to solutions to tune the arrangement of surfactants on their surface. Depending on the mixture, selected CNTs turn highly hydrophobic or hydrophilic, separating them from the rest of the mixture.

Fluorescence in carbon nanotubes is the product of absorption at the excitation frequency, corresponding to the second Van Hove optical transition (E22) , labeled in Fig.4.2(c), from the valence to conduction bands, followed by relaxation to the first Van Hove optical transition (E11) from the conduction to valence band. The corresponding excitation and emission wavelengths can be as a function of diameter in nanometers and chiral angle are

degrees derived in [44]. The parameters fitted differ along CNT groups, having to do with chiral number differences: $(n-m) \bmod 3 = 1$ is group 1, $(n-m) \bmod 3 = 2$ is group 2, $(n-m) \bmod 3 = 0$ are metallic CNTs and do not fluoresce and so are excluded.

For group 1:

$$(Emission)\lambda_{11} = \left[\frac{10^7(cm^{-1})}{157.5 + 1066.9d_t} - A_{1m1}(cm^{-1}) \frac{\cos(3\theta)^{1.374}}{d_t^{2.272}} \right]^{-1} \quad (4.10)$$

$$(Excitation)\lambda_{22} = \left[\frac{10^7(cm^{-1})}{145.6 + 575.7d_t} + A_{2m1}(cm^{-1}) \frac{\cos(3\theta)^{0.828}}{d_t^{1.809}} \right]^{-1} \quad (4.11)$$

For group 2:

$$(Emission)\lambda_{11} = \left[\frac{10^7(cm^{-1})}{157.5 + 1066.9d_t} + A_{1m2}(cm^{-1}) \frac{\cos(3\theta)^{0.886}}{d_t^{2.129}} \right]^{-1} \quad (4.12)$$

$$(Excitation)\lambda_{22} = \left[\frac{10^7(cm^{-1})}{145.6 + 575.7d_t} - A_{2m2}(cm^{-1}) \frac{\cos(3\theta)^{1.110}}{d_t^{2.497}} \right]^{-1} \quad (4.13)$$

Additional parameters $A_{1m1}, A_{1m2}, A_{2m1}, A_{2m2}$, account for variations of spectrum in same diameter CNTs. Not all variation differences are yet explained but comparison of aqueous solutions[48][43] found spectral shifts of 2%.

Plots of the excitation-emission spectrum are using variational parameters from fitting to data of samples of individual SWNT in aqueous sodium dodecyl sulfate (SDS)[43] are shown in Fig.4.3. Group 1 CNTs have lower Stokes shifts, and small chiral angles ($< 2^\circ$) while group 2 have higher Stokes shift and span full 0° to 30° chiral angle range with similar angles along chiral number difference ($n - m$). Regardless of group, the in excitation and emission wavelengths increase with diameter.

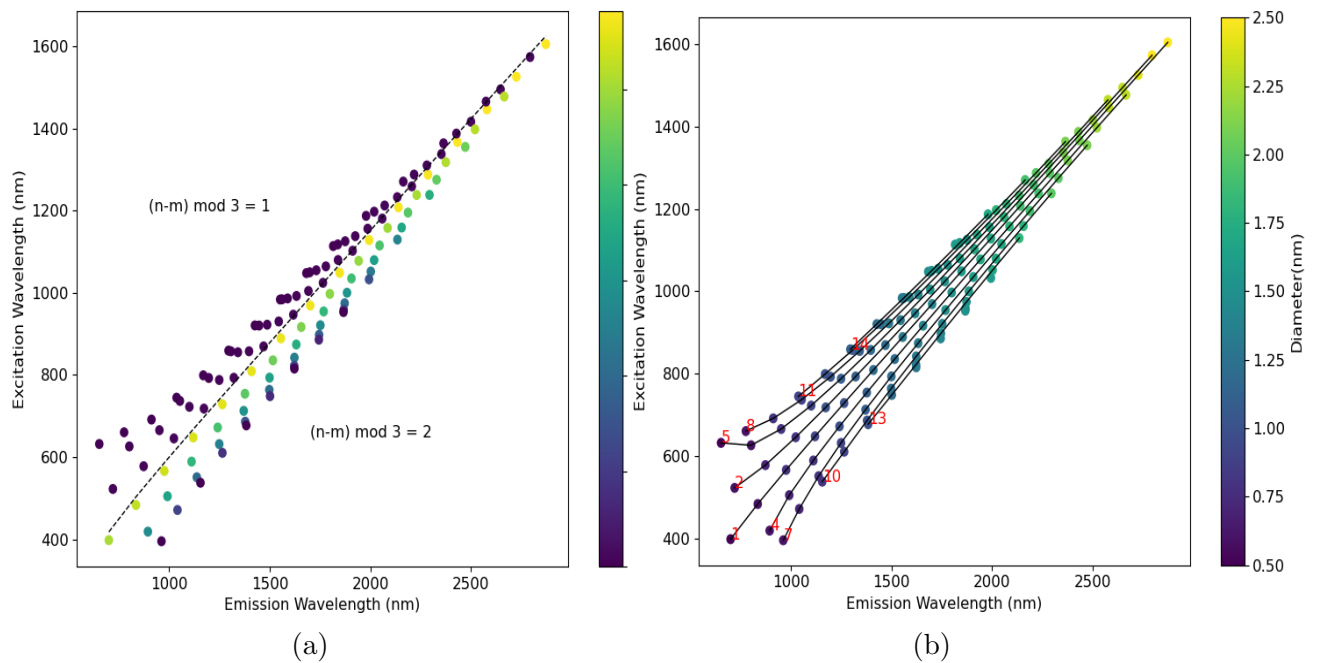


Figure 4.3: Group characteristics of CNTs colored by using variational parameters from [43], valid for diameters $> 0.5\text{nm}$. Color spectrum of plot denoting (a)chiral angle and (b)diameter. Increase in Stokes shifts with diameter along chiral difference $(n - m)$ lines, noted in red and connected by black lines.

4.4 HCPCF Bandgap Overlap with CNT Excitation and Emission

To successfully collect the CNT fluorescence when suspended within a HCPCF, the particle emission and excitation must be within the bandgap of the fiber. Taking the most commonly available HCPCFs, Table 4.1 shows the central operating wavelengths for core-filled and fully D₂O-filled fibers. In Fig.4.4, the liquid-filled HCPCF bandgaps are overplayed with the excitation and emission spectrums of CNTs calculated in the previous section. From this overlay, it appears that 10 chiralities of CNTs fall within the bandgap of a fully-filled 1550nm HCPCF and one within the bandgap of fully-filled 1060nm HCPCF. The potential CNT candidates and their characteristics are listed in Table 4.2 along and their spectrum plotted within the 1550nm fully-filled bandgap in Fig.4.5.

HCPCF	λ_{Core} (nm)	$\lambda_{D_2O Shifted}$ (nm)	Range (nm)
HC2000	2000	1144	250
HC1550	1550	887	500
HC1060	1060	606	100
HC800B	800	457	200

Table 4.1: Thorlabs fiber bandgap shift. The ranges for HC1550 and HC800B are approximated from spectrum measurements and HC2000 and HC1060 are taken from NKT datasheets[53, 54].

QuIN Lab at the University of Waterloo has developed a CNT isolation process using the surfactant sodium deoxycholate (DOC) in DI water, and are able to produce samples with (7, 6) and (7, 5) dominant samples. Thus far an experiential set-up for characterizing the CNT samples was completed, but use of the sample in HCPCF has not yet been completed. The sample information that has so far been collected is included.

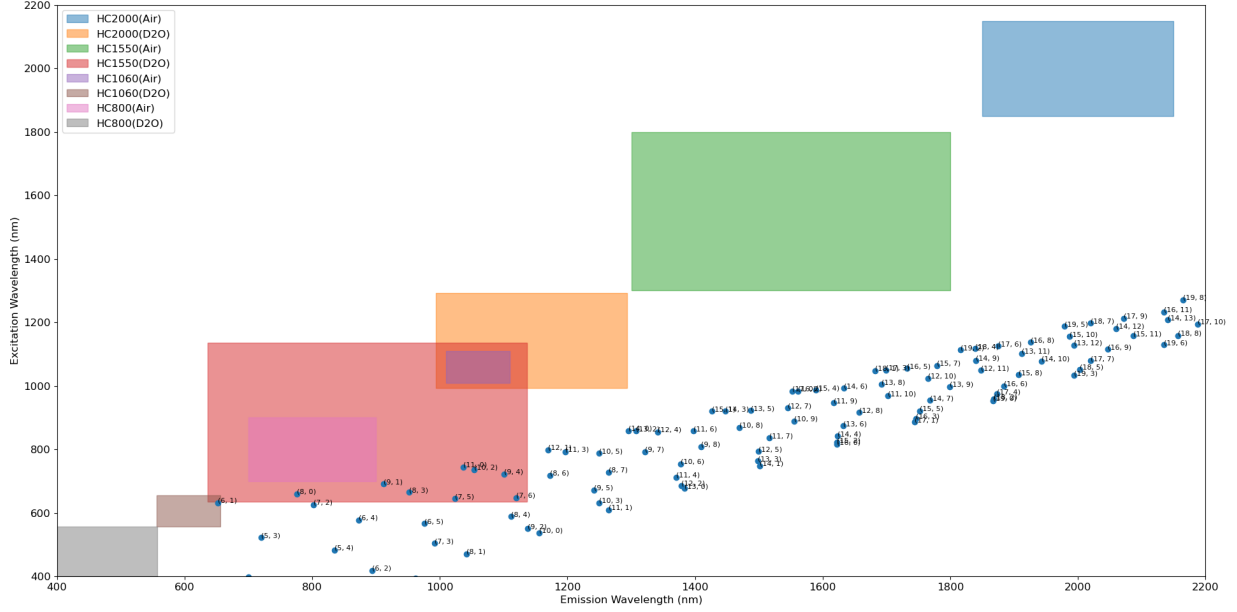


Figure 4.4: Hollow-core fiber bandgap overlayed on CNT emission vs. excitation wavelengths

(n, m)	dt (nm)	Θ (deg)	λ_{11} (nm)	λ_{22} (nm)
(6, 1)	0.52	0.13	652.62	631.79
(7, 2)	0.65	0.21	802.05	625.92
(7, 5)	0.83	0.43	1023.74	645.33
(7, 6)	0.89	27.46	1119.76	647.64
(8, 0)	0.64	0	776.01	660.25
(8, 3)	0.78	0.27	951.61	665.39
(9, 1)	0.76	0.09	912.1	691.29
(9, 4)	0.92	0.31	1100.63	722.39
(10, 2)	0.88	0.16	1053.43	736.68
(11, 0)	0.87	0	1036.93	744.57

Table 4.2: CNTs with emission and excitation transmittable through HC1550 filled with D₂O.

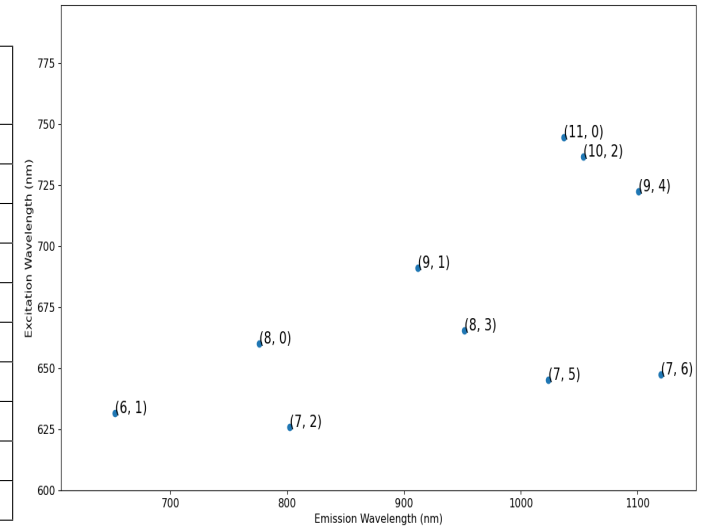


Figure 4.5: Excitation/Emission spectrum of CNTs falling within the D₂O-filled 1550HCPCF bandgap.

4.4.1 Experiment Set-Up

A tunable, few nanometer linewidth light source for excitation wavelengths between 600 – 700nm was made by passing a super continuum source through a diffraction grating and filtering through an optical slit. The full set-up used to measure absorption and fluorescence of the sample is shown in Fig.4.6.

Sample History

CNT samples were prepared by HeeBong Yang from the QuIN Lab at the University of Waterloo. SG65i powder was purchased from Sigma Aldrich and Dispersed in a surfactant at an initial powder concentration of 1 mg/mL. The sample then underwent a procedure of purification steps, sorting with polymers & surfactants, and polymer exchange. The final condition of the sample was 65% (7,5), (7,6) dominant SWCNTs in DI water with 0.04% DOC, but at an unknown concentration.

Sample Characteristics

CNT solutions follow Beer-Lambert's Law [57, 60], $A = \log\left(\frac{I_{in}}{I_{out}}\right) = \varepsilon CL$ so the concentration can be deduced from the measured absorbance. Fig.4.7(a) and the average previously reported extinction coefficient[58, 59, 60] $\varepsilon = 30.98 \text{ mL mg}^{-1}\text{cm}^{-1}$ estimate a sample concentration around $0.0042 \pm 0.0007 \text{ mg/mL}$.

Unfortunately no PL was detected from the sample. Despite the high absorption loss from DI water in the excitation wavelength range, fluorescence has been detected for these chiralities of CNTs suspended in DI water before[56], though there is 23.25% pm 10% decrease in PL intensity when using H₂O instead of D₂O for (7, 5) and 42.5% pm 5% for (7,6) % and quantum yields are expected to be around 1.04% and 1.40% respectively. The next steps to preclude the source of quenching in the CNT sample is to measure the absorption with various thicknesses of cuvette or to incrementally dilute the sample.

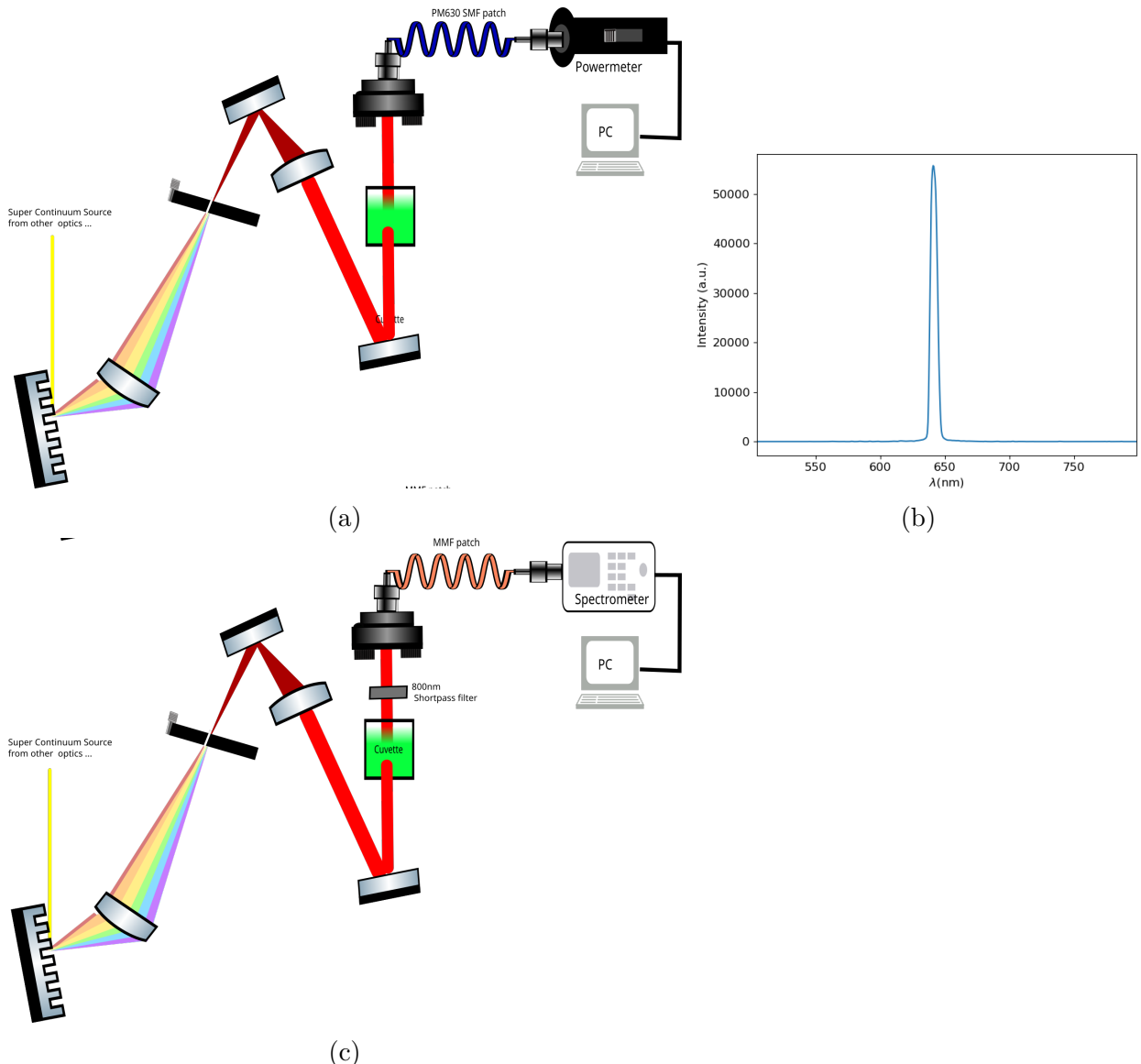


Figure 4.6: The experiential used set-up for measuring (a)Absorption and (c) Fluorescence of CNT samples in a cuvette. (b)The spectrum and intensity of the excitation beam at $\lambda = 645\text{nm}$ picked-off the super continuum source. The power measures $48\mu\text{W}$ and $\text{fwhm}=6\text{nm}$.

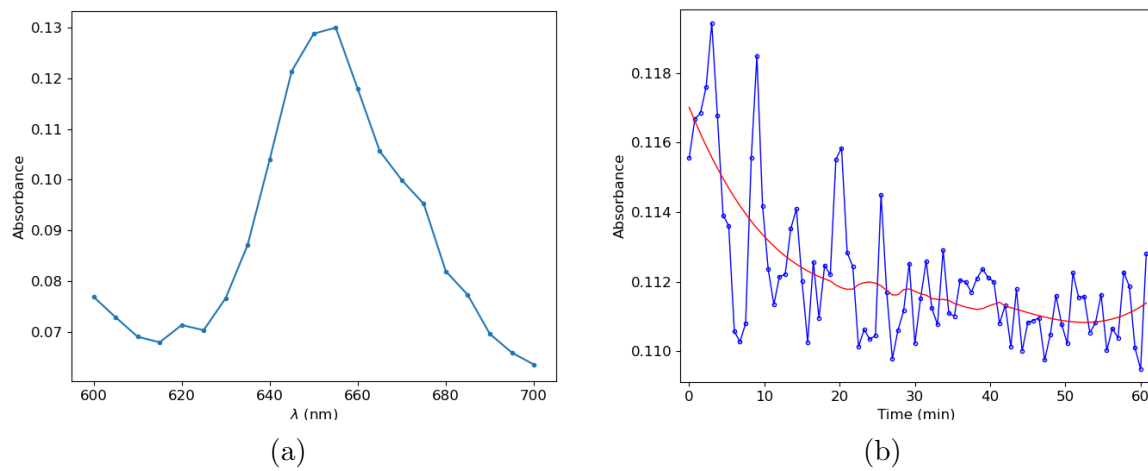


Figure 4.7: (a) Absorbance spectrum of CNT sorted CNT sample (b)Absorbance of CNT sorted sample over 60 minutes, the absorbance of the sample stabilizes after 30 minutes.

Chapter 5

Conclusion

In this thesis use of HCPCFs as a liquid-waveguide was studied. The preservation of light bandgap guidance through liquid demonstrated by experimentally confirming the scaling laws for liquid-filled fibers of H₂O and D₂O. The main results of the thesis were obtained in the measurements of the interaction of suspended ICG particles within the mode of the fiber. The dye molecules were excited in the fiber and fully-filled HCPCF guiding light via optical bandgap exhibited a higher efficiency than that seen in the liquid-core fiber. Despite difficulty with the coupling, there is high enough efficiency the potential of creating fluorescent light sources. However, using organic molecules becomes troublesome due to rapid degradation and photobleaching. Semiconducting CNTs in theory can also be used as a fluorescent medium, removing the lifespan issues of organic dyes and increased tunability through chirality selection processes. The overlap in certain chirality CNT spectrums and the bandgap of commercially available HCPCF when filled with heavy water makes further study into their integration warranted.

Future Work

While the results of suspended ICG particles are promising and show a proof-of-concept, the progression to suspended CNTs in HCPCF is incomplete. The initial tests with a sorted CNTs sample were inconclusive and further investigation is needed to produce a fluorescent sample. Future experimental efforts will hopefully lead to uses of CNTs in fiber-integrated devices. Besides the CNT samples, one of the main challenges that remains is obtaining a consistent and high coupling to the 1550nm HCPCF. Butt-coupled mechanical splicing chips fabricated for 800nm HCPCF consistently achieve coupling around 75-80% and robustly hold the fibers together[9], but the same recipe does not produce high-fidelity butt-coupled mechanical splicing chips for 1550nm HCPCF. This is another avenue that

needs to be explored but it is likely to be solved with modest efforts.

After the implementation of the aforementioned improvements, future prospects include integrating the suspended particle-filled HCPCF into a narrow linewidth external cavity semiconductor laser (NLECSL) as a gain medium. A potential NLECSL set-up using the common Littrow configuration depicted in Fig.5.1(a). Narrow line-width dye lasers have

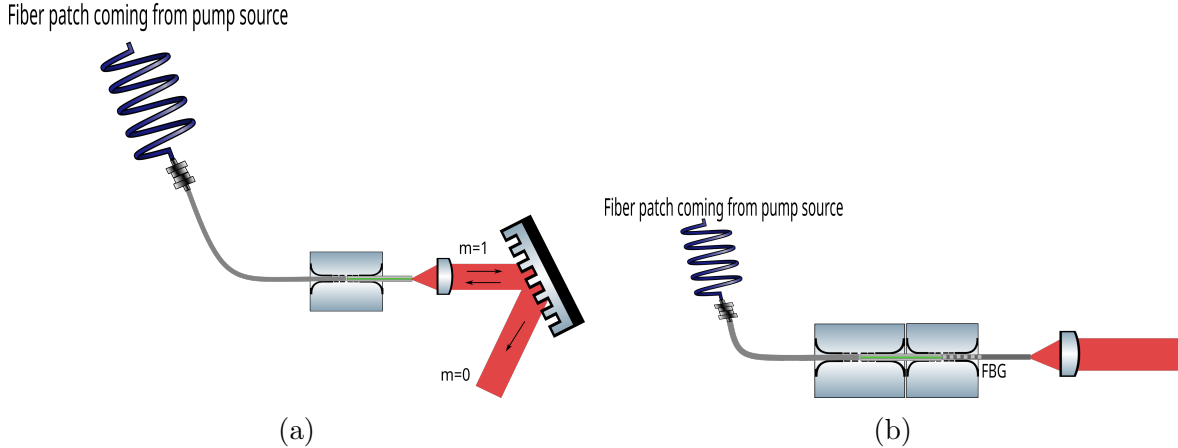


Figure 5.1: Example NLECSL configurations integrating the liquid-HCPCF as the gain medium (a) Littrow configuration (b) Single-wavelength fiber-integrated approach with FBG.

already been made using liquid dyes as gain medium[64, 63] with applications nonlinear[66] and atomic optics[67]. With organic dyes like ICG having wide fluorescence spectrum a tunable laser is desirable, but CNTs typically have fluorescence linewidth around 4-6nm when isolated and 20nm in bulk samples[61] will have promise in a fixed-wavelength cavity. For single-wavelength laser configurations, fiber-integrated systems have been demonstrated using fiber Bragg-gratings as end-reflector of an external cavity system[62]. An easy integration if using fiber splicing chips Fig.5.1(b).

References

- [1] Yariv, Amnon and Pochi Albert Yeh, Optical Waves in Crystals: Propagation and Control of Laser Radiation,” 1st ed. Wiley-Interscience, 2002.
- [2] J. D. Joannopoulos, Photonic crystals: molding the flow of light, 2nd ed. Princeton: Princeton University Press, 2008.
- [3] R. K. Chourasia and V. Singh, “Estimation of photonic band gap in the hollow core cylindrical multilayer structure,” *Superlattices and Microstructures*, vol. 116, pp. 191–199, Apr. 2018, doi: 10.1016/j.spmi.2018.02.023.
- [4] P. R. Villeneuve and M. Piche’, “Photonic band gaps in two-dimensional square and hexagonal lattices,” *Phys. Rev. B*, vol. 46, no. 8, pp. 4969–4972, Aug. 1992, doi: 10.1103/PhysRevB.46.4969.
- [5] R. F. Cregan et al., “Single-Mode Photonic Band Gap Guidance of Light in Air,” *Science*, vol. 285, no. 5433, pp. 1537–1539, Sep. 1999, doi: 10.1126/science.285.5433.1537.
- [6] I. A. Sukhoivanov and I. V. Guryev, Photonic Crystals: Physics and Practical Modeling, vol. 152. Berlin, Heidelberg: Springer Berlin Heidelberg, 2009. doi: 10.1007/978-3-642-02646-1.
- [7] T. A. Birks, D. M. Bird, T. D. Hedley, J. M. Pottage, and P. St. J. Russell, “Scaling laws and vector effects in bandgap-guiding fibres,” *Opt. Express*, vol. 12, no. 1, p. 69, 2004, doi: 10.1364/OPEX.12.000069.
- [8] G. Antonopoulos, F. Benabid, T. A. Birks, D. M. Bird, J. C. Knight, and P. St. J. Russell, “Experimental demonstration of the frequency shift of bandgaps in photonic crystal fibers due to refractive index scaling,” *Opt. Express*, vol. 14, no. 7, p. 3000, 2006, doi: 10.1364/OE.14.003000.
- [9] R. A. Maruf and M. Bajcsy, “On-chip splicer for coupling light between photonic crystal and solid-core fibers,” *Appl. Opt.*, vol. 56, no. 16, p. 4680, Jun. 2017.

- [10] L. Xiao, W. Jin, M. S. Demokan, H. L. Ho, Y. L. Hoo, and C. Zhao, “Fabrication of selective injection microstructured optical fibers with a conventional fusion splicer,” Opt. Express, vol. 13, no. 22, p. 9014, 2005.
- [11] S. Kedenburg, M. Vieweg, T. Gissibl, and H. Giessen, “Linear refractive index and absorption measurements of nonlinear optical liquids in the visible and near-infrared spectral region,” Opt. Mater. Express, vol. 2, no. 11, p. 1588, Nov. 201
- [12] M. Bajcsy et al., “Laser-cooled atoms inside a hollow-core photonic-crystal fiber,” Phys. Rev. A, vol. 83, no. 6, p. 063830, Jun. 2011, doi: 10.1103/PhysRevA.83.063830.
- [13] A. P. Hilton, C. Perrella, F. Benabid, B. M. Sparkes, A. N. Luiten, and P. S. Light, “High-efficiency cold-atom transport into a waveguide trap,” Phys. Rev. Applied, vol. 10, no. 4, p. 044034, Oct. 2018, doi: 10.1103/PhysRevApplied.10.044034. A
- [14] P. Domokos, P. Horak, and H. Ritsch, “Quantum description of light-pulse scattering on a single atom in waveguides,” Phys. Rev. A, vol. 65, no. 3, p. 033832, Mar. 2002, doi: 10.1103/PhysRevA.65.033832.
- [15] M. T. Manzoni, “New Systems for Quantum Nonlinear Optics,” . 2017, Thesis, p. 39-40.
- [16] X. Fang et al., “One-step condensation synthesis and characterizations of indocyanine green,” Results in Chemistry, vol. 3, p. 100092, Jan. 2021, doi: 10.1016/j.rechem.2020.100092.
- [17] W. Holzer et al., ”Photostability and thermal stability of indocyanine green,” Journal of Photochemistry and Photobiology B: Biology, vol. 47, no. 2-3, pp. 155-164, Dec. 1998.
- [18] M. L. Landsman, G. Kwant, G. A. Mook, and W. G. Zijlstra, “Light-absorbing properties, stability, and spectral stabilization of indocyanine green,” Journal of Applied Physiology, vol. 40, no. 4, pp. 575–583, Apr. 1976.
- [19] M. Mauerer, A. Penzkofer, and J. Zweck, “Dimerization, J-aggregation and J-disaggregation dynamics of indocyanine green in heavy water,” Journal of Photochemistry and Photobiology B: Biology, vol. 47, no. 1, pp. 68–73, Nov. 1998.
- [20] F. Rotermund, R. Weigand, W. Holzer, M. Wittmann, and A. Penzkofer, “Fluorescence spectroscopic analysis of indocyanine green J aggregates in water,” Journal of Photochemistry and Photobiology A: Chemistry, vol. 110, no. 1, pp. 75–78, Oct. 1997.

- [21] R. Philip, A. Penzkofer, W. Bäumler, R. M. Szeimies, and C. Abels, “Absorption and fluorescence spectroscopic investigation of indocyanine green,” *Journal of Photochemistry and Photobiology A: Chemistry*, vol. 96, no. 1–3, pp. 137–148, May 1996.
- [22] V. Saxena, M. Sadoqi, and J. Shao, “Degradation Kinetics of Indocyanine Green in Aqueous Solution,” *Journal of Pharmaceutical Sciences*, vol. 92, no. 10, pp. 2090–2097, Oct. 2003.
- [23] D. Farrakhova et al., “Fluorescence imaging analysis of distribution of indocyanine green in molecular and nanoform in tumor model,” *Photodiagnosis and Photodynamic Therapy*, vol. 37, p. 102636, Mar. 2022, doi: 10.1016/j.pdpdt.2021.102636.
- [24] E. Spartalis et al., “Intraoperative Indocyanine Green (ICG) Angiography for the Identification of the Parathyroid Glands: Current Evidence and Future Perspectives,” *In Vivo*, vol. 34, no. 1, pp. 23–32, 2020, doi: 10.21873/invivo.11741.
- [25] D. J. DeDora et al., “Sulfobutyl ether β -cyclodextrin and methyl β -cyclodextrin enhance and stabilize fluorescence of aqueous indocyanine green: Sulfobutyl Ether β -Cyclodextrin and METHYL β -Cyclodextrin,” *J. Biomed. Mater. Res.*, vol. 104, no. 7, pp. 1457–1464, Oct. 2016, doi: 10.1002/jbm.b.33496.
- [26] R. Weigand, F. Rotermund, and A. Penzkofer, “Degree of aggregation of indocyanine green in aqueous solutions determined by Mie scattering,” *Chemical Physics*, vol. 220, no. 3, pp. 373–384, Aug. 1997, doi: 10.1016/S0301-0104(97)00150-X.
- [27] P. C. Hiemenz and R. D. Vold, “Particle size from the optical properties of flocculating carbon dispersions,” *Journal of Colloid and Interface Science*, vol. 21, no. 5, pp. 479–488, May 1966, doi: 10.1016/0095-8522(66)90046-8.
- [28] A. J. Cox, A. J. DeWeerd, and J. Linden, “An experiment to measure Mie and Rayleigh total scattering cross sections,” *American Journal of Physics*, vol. 70, no. 6, pp. 620–625, Jun. 2002, doi: 10.1119/1.1466815.
- [29] D. V. Vezenov, B. T. Mayers, D. B. Wolfe, and G. M. Whitesides, “Integrated fluorescent light source for optofluidic applications,” *Appl. Phys. Lett.*, vol. 86, no. 4, p. 041104, Jan. 2005, doi: 10.1063/1.1850610.
- [30] C. L. Bliss, J. N. McMullin, and C. J. Backhouse, “Integrated wavelength-selective optical waveguides for microfluidic-based laser-induced fluorescence detection,” *Lab Chip*, vol. 8, no. 1, pp. 143–151, 2008, doi: 10.1039/B711601B.

- [31] R. S. Conroy, B. T. Mayers, D. V. Vezenov, D. B. Wolfe, M. G. Prentiss, and G. M. Whitesides, “Optical waveguiding in suspensions of dielectric particles,” p. 5.
- [32] A. Cusano et al., “Optical probes based on optical fibers and single-walled carbon nanotubes for hydrogen detection at cryogenic temperatures,” *Appl. Phys. Lett.*, vol. 89, no. 20, p. 201106, Nov. 2006, doi: 10.1063/1.2370292.
- [33] S. Dresselhaus, “PHYSICS OF CARBON NANOTUBES,” *Carbon*, 33(7), 883-891, 1995.
- [34] V. Popov, “Carbon nanotubes: properties and application,” *Materials Science and Engineering: R: Reports*, vol. 43, no. 3, pp. 61–102, Jan. 2004.
- [35] S. Yamashita, “Nonlinear optics in carbon nanotube, graphene, and related 2D materials,” *APL Photonics*, vol. 4, no. 3, p. 034301, Mar. 2019.
- [36] R. Saito, M. Fujita, G. Dresselhaus, and M. S. Dresselhaus, “Electronic structure of chiral graphene tubules,” *Appl. Phys. Lett.*, vol. 60, no. 18, pp. 2204–2206, May 1992.
- [37] C. Thomsen, S. Reich, and J. Maultzsch, *Carbon Nanotubes: Basic Concepts and Physical Properties*, 1st ed. Wiley, 2004.
- [38] H. Kataura et al., “Optical properties of single-wall carbon nanotubes,” *Synthetic Metals*, vol. 103, no. 1–3, pp. 2555–2558, Jun. 1999.
- [39] R. Saito, G. Dresselhaus, and M. S. Dresselhaus, “Trigonal warping effect of carbon nanotubes,” *Phys. Rev. B*, vol. 61, no. 4, pp. 2981–2990, Jan. 2000, doi: 10.1103/PhysRevB.61.2981.
- [40] S. Maruyama, Fullerene and Carbon Nanotube Site [Online]. Available: <http://www.photon.t.u-tokyo.ac.jp/maruyama/nanotube.html>
- [41] S. Yamashita, “A Tutorial on Nonlinear Photonic Applications of Carbon Nanotube and Graphene,” *J. Lightwave Technol.*, vol. 30, no. 4, pp. 427–447, Feb. 2012.
- [42] A. Gambetta et al., “Sub-100 fs two-color pump-probe spectroscopy of Single Wall Carbon Nanotubes with a 100 MHz Er-fiber laser system,” p. 8, 2008.
- [43] R. B. Weisman and S. M. Bachilo, “Dependence of Optical Transition Energies on Structure for Single-Walled Carbon Nanotubes in Aqueous Suspension: An Empirical Kataura Plot,” *Nano Lett.*, vol. 3, no. 9, pp. 1235–1238, Sep. 2003.

- [44] S. M. Bachilo, M. S. Strano, C. Kittrell, R. H. Hauge, R. E. Smalley, and R. B. Weisman, “Structure-Assigned Optical Spectra of Single-Walled Carbon Nanotubes,” *Science*, vol. 298, no. 5602, pp. 2361–2366, Dec. 2002.
- [45] S. Giordani et al., “Debundling of Single-Walled Nanotubes by Dilution: Observation of Large Populations of Individual Nanotubes in Amide Solvent Dispersions,” *J. Phys. Chem. B*, vol. 110, no. 32, pp. 15708–15718, Aug. 2006.
- [46] A. Martinez and S. Yamashita, “Carbon Nanotube-Based Photonic Devices: Applications in Nonlinear Optics,” In: J. M. Marulanda, Ed., *Carbon Nanotubes Applications on Electron Devices*, InTech, 2011.
- [47] Vl. A. Margulis and T. A. Sizikova, “Theoretical study of third-order nonlinear optical response of semiconductor carbon nanotubes,” *Physica B: Condensed Matter*, vol. 245, no. 2, pp. 173–189, Mar. 1998.
- [48] E. Turek, T. Shiraki, T. Shiraishi, T. Shiga, T. Fujigaya, and D. Janas, “Single-step isolation of carbon nanotubes with narrow-band light emission characteristics,” *Sci Rep*, vol. 9, no. 1, p. 535, Dec. 2019
- [49] M. Chernysheva et al., “Carbon nanotubes for ultrafast fibre lasers,” *Nanophotonics*, vol. 6, no. 1, pp. 1–30, Jan. 2017, doi: 10.1515/nanoph-2015-0156.
- [50] C. S. Goh et al., “Femtosecond mode-locking of a ytterbium-doped fiber laser using a carbon-nanotube-based mode-locker with ultra-wide absorption band,” in (CLEO). Conference on Lasers and Electro-Optics, 2005., Baltimore, MD, USA, 2005, pp. 1644-1646 Vol. 3. doi: 10.1109/CLEO.2005.202227.
- [51] K. Kieu and F. W. Wise, “All-fiber normal-dispersion femtosecond laser,” *Opt. Express*, vol. 16, no. 15, p. 11453, Jul. 2008, doi: 10.1364/OE.16.011453.
- [52] Y. Z. Pan, J. G. Miao, W. J. Liu, X. J. Huang, and Y. B. Wang, “Mode-locked ytterbium fiber lasers using a large modulation depth carbon nanotube saturable absorber without an additional spectral filter,” *Laser Phys. Lett.*, vol. 11, no. 9, p. 095105, Sep. 2014, doi: 10.1088/1612-2011/11/9/095105.
- [53] NKT Photonics, “2 μ m Range Hollow Core Photonic Bandgap Fiber,” HC-2000-01.
- [54] NKT Photonics, “Hollow Core Photonic Bandgap Fiber for 1060nm Range Applications,” HC-1060-02.

- [55] A. Hendler-Neumark and G. Bisker, “Fluorescent Single-Walled Carbon Nanotubes for Protein Detection,” Sensors, vol. 19, no. 24, p. 5403, Dec. 2019, doi: 10.3390/s19245403.
- [56] X. Wei et al., “Photoluminescence Quantum Yield of Single-Wall Carbon Nanotubes Corrected for the Photon Reabsorption Effect,” p. 23.
- [57] F. Schöppler et al., “Molar Extinction Coefficient of Single-Wall Carbon Nanotubes,” J. Phys. Chem. C, vol. 115, no. 30, pp. 14682–14686, Aug. 2011, doi: 10.1021/jp205289h.
- [58] A. J. Blanch, C. E. Lenehan, and J. S. Quinton, “Parametric analysis of sonication and centrifugation variables for dispersion of single walled carbon nanotubes in aqueous solutions of sodium dodecylbenzene sulfonate,” Carbon, vol. 49, no. 15, pp. 5213–5228, Dec. 2011, doi: 10.1016/j.carbon.2011.07.039.
- [59] A. Ansón-Casaos, J. M. González-Domínguez, I. Lafragüeta, J. A. Carrodeguas, and M. T. Martínez, “Optical absorption response of chemically modified single-walled carbon nanotubes upon ultracentrifugation in various dispersants,” Carbon, vol. 66, pp. 105–118, Jan. 2014, doi: 10.1016/j.carbon.2013.08.048.
- [60] S. H. Jeong, K. K. Kim, S. J. Jeong, K. H. An, S. H. Lee, and Y. H. Lee, “Optical absorption spectroscopy for determining carbon nanotube concentration in solution,” Synthetic Metals, vol. 157, no. 13–15, pp. 570–574, Jul. 2007, doi: 10.1016/j.synthmet.2007.06.012.
- [61] D. A. Tsyboulski, J.-D. R. Rocha, S. M. Bachilo, L. Cognet, and R. B. Weisman, “Structure-Dependent Fluorescence Efficiencies of Individual Single-Walled Carbon Nanotubes,” Nano Lett., vol. 7, no. 10, pp. 3080–3085, Oct. 2007, doi: 10.1021/nl071561s.
- [62] K. Ding et al., “Research on Narrow Linewidth External Cavity Semiconductor Lasers,” Crystals, vol. 12, no. 7, p. 956, Jul. 2022, doi: 10.3390/crust12070956.
- [63] F. J. Duarte, Ed., Organic Lasers and Organic Photonics, Bristol, IOP, 2018. doi: 10.1007/978-3-662-11579-4.
- [64] F. P. Schäfer, Ed., Dye Lasers, vol. 1. Berlin, Heidelberg: Springer Berlin Heidelberg, 1973. doi: 10.1007/978-3-662-11579-4.

- [65] B. Pierce and R. Birge, "Lasing properties of several near-IR dyes for a nitrogen laser-pumped dye laser with an optical amplifier," *IEEE J. Quantum Electron.*, vol. 18, no. 7, pp. 1164–1170, Jul. 1982, doi: 10.1109/JQE.1982.1071672.
- [66] Robert A. Norwood, "Organic Photonics: Ready for Prime Time," *Optics & Photonics News* 24(11), 40-47, 2013.
- [67] M. Stuke, *Dye Lasers: 25 Years*. Berlin, Heidelberg: Springer-Verlag Springer, ch.11, 2005.